Thermoelectric Properties of Ternary Tellurides and Quaternary Derivative of Tl_9BiTe_6

by

Tinting Mu

A thesis
presented to the University of Waterloo
in fulfillment of the
thesis requirement for the degree of
Master of Science
in
Chemistry

Waterloo, Ontario, Canada, 2010

Declaration

I hereby declare that I am the sole author of this thesis. This is a true copy of the thesis, including any required final revisions, as accepted by my examiners.

I understand that my thesis may be made electronically available to the public.

Abstract

The main focus of this work was on exploratory preparation of thermoelectric materials and analyses of their physical properties. A thermoelectric material is capable of converting heat to electricity or vice versa. Usually, narrow band gap semiconductors are good candidates for thermoelectric applications, because such materials have large Seebeck coefficient, reasonably high electrical conductivity and low thermal conductivity. In this work, two different systems were studied, ternary layered tellurides and quaternary derivatives of Tl_9BiTe_6. I tried to prepare $Pb_{1-x}Bi_{2+x}Te_4$ with x = 0.30, 0.10, –0.10 and = 0.30 and $Pb_{1-x}Bi_{4+x}Te_7$ with x = 0.15, 0.00, –0.15 and –0.35, and two pure compounds, $Pb_{0.8}Bi_{2.2}Te_4$ and $Pb_{0.9}Bi_{2.1}Te_4$ were obtained. Powder X-ray diffraction was used to confirm the purity of the compounds, and physical properties were measured on cold-pressed samples with densities around 80% of the theoretical value. The figure of merit of the ternary tellurides is comparable to the published values of $PbBi_2Te_4$ (0.5 at 600 K). I also investigated the quaternary series $Tl_{8.67}Pb_xBi_{1.33-x}Te_6$ with x between 0.50 and 1.00. The purity was confirmed by powder X-ray diffraction data, and physical properties were measured on Spark Plasma Sintered (SPS) samples. Low thermal conductivity was observed as well as competitive power factors. The highest ZT value was 0.57 for the compound $Tl_{8.67}Pb_{0.60}Bi_{0.73}Te_6$ at 575 K.

Acknowledgements

I am heartily thankful to my supervisor, Dr. Holger Kleinke, whose encouragement, guidance and support from the initial to the final level enabled me to develop an understanding of my research.

I would like to express my sincere gratitude to my committee members, Dr. Linda Nazar, Dr. Eric Prouzet and Dr. Dmitriy Soldatov for their important support throughout this work.

I wish to thank Dr. James R. Salvador, Dr. Jihui Yang and Dr. Gregory P. Meisner of the General Motors R&D center for valuable discussions.

I am also grateful to Dr. Gianluigi Botton and David Rossouw for providing us with the HRTEM data and discussion.

Lastly, the financial support of General Motors of Canada and NSERC is gratefully acknowledged.

Table of Contents

List of Figures

List of Tables

1. Introduction

In December, 2009, the United Nations' two-week conference on climate change was hosted in Copenhagen in order to prevent dangerous levels of global warming. However, the summit could not come to a satisfying agreement in the end[1]. This is in part caused by our limited natural resources and unavoidable environmental pollutions during manufacture processes. Nowadays, humans still greatly depend on the finite sources of fossil fuels. How we can reduce dependency on the fossil fuels and therefore lessen the green house emission becomes the biggest concern all over the world. It also becomes the motivation for finding replacements of conventional sources of energies. For decades, great progress has been made in research on solar cells[2], wind turbines[3], fuel cells[4] and so on. The thesis focuses on thermoelectric materials which are capable of converting heat to electricity or vice versa[5].

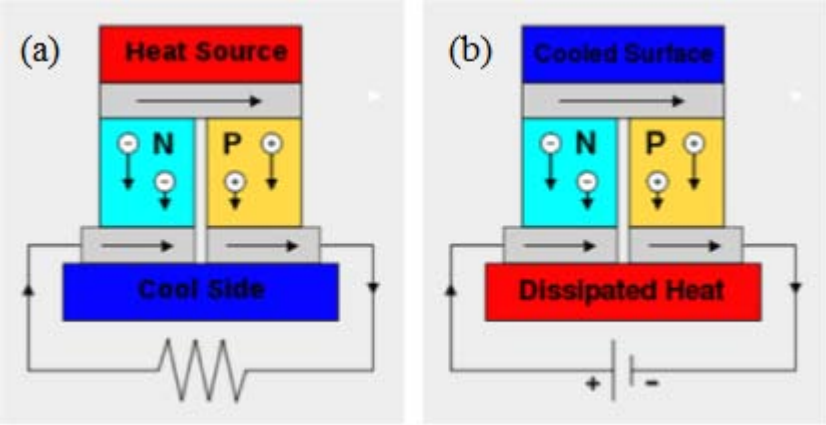

Figure 1.1 Thermoelectric (a) power generation; and (b) refrigeration[5].

In 1821, German physicist Thomas Johann Seebeck found that a compass would deflect near a closed loop made from two dissimilar metals with junctions at different temperature[5]. This was due to the temperature difference at the junctions, which induced a current along the closed loop, and therefore, by Ampere's law, deflected the compass. Such phenomenon is called the Seebeck effect. It can be considered that the free electrons with enough kinetic energy (thermal energy) tend to travel from one junction to the other, and therefore a potential difference is created between the two junctions[5]. The two metals can be characterized as n-type (electron carriers) or p-type (holes) (Figure 1.1). Materials with high thermoelectric figure-of-merit are semiconductors with optimized doping levels, such as tellurides of antimony and bismuth. In the past several decades, scientists have been achieved a great

success in increasing the efficiency of thermoelectric generators.

Energy demands of our society keep increasing. One of the advantages of thermoelectric materials is that they are environmental friendly. They are capable of converting waste heat (e.g. fuel consumption of the automotives) generated from our daily life. Secondly, a thermoelectric power generator is extremely important when no energy available other than thermal energy (e.g. in a spacecraft in the outer space). Moreover, since thermoelectric devices usually do not have moving parts, they require very limited maintenance. Furthermore, by adjusting temperature, thermoelectric devices can be easily controlled. Nevertheless, thermoelectric materials have not been applied in waste heat recovery, because most conventional thermoelectric modules are low in efficiencies. In recent years, newly discovered thermoelectric materials have exhibited improvement in thermoelectric properties, resulting in higher efficiencies. The following sections will focus on a brief introduction to thermoelectric materials and applications, parameters which influence the properties, and finally some of the latest achievements in this field.

1.1 Development of Thermoelectric Materials

1.1.1 Discovery of Thermoelectric Materials

Thermoelectric effect refers collectively to the Seebeck effect, Peltier effect, and the Thomson effect. The Seebeck effect is named after the German physicist Thomas Johann Seebeck. He discovered that a compass would be deflected by a circuit made from two dissimilar metals, with junctions at different temperatures. However, Seebeck was not the one who realized that this is due to an electric current induced by the temperature differences between the junctions[5]. The Danish physicist Hans Christian Ørsted was the one who tried to explain and conceive the term 'thermoelectricity'. The thermoelectric effect arises because the temperature differences at the junctions make electrons tend to accumulate at one side over the other. Hence a potential difference is built up. In 1834, The Peltier effect was discovered by Jean-Charles Peltier, a French physicist[5]. This effect can be considered as the reverse process of the Seebeck effect. When a current is made to flow through a circuit made from two different metals, a calorific effect can be detected at one junction. Later in 1851, William Thomson predicted and experimentally observed that any current-carrying conductor, with a temperature difference between two junctions, will either absorb or emit heat[6]. Thomson provided a comprehensive explanation of the Seebeck and Peltier effects and described their interrelationship.

1.1.2 Power Generation and Refrigeration

Thermoelectric devices are mainly used for the power generation and refrigeration. Thermoelectric power sources have proven their extraordinary reliability and longevity for outer space missions (67 missions to date, more than 30 years of life)[7]. An example of a successful application of the thermoelectric generator is shown in Figure 1.2. Thermoelectric power sources are extremely important when there is exclusive of other sources, or in unmanned or unmaintained situations, such as in space missions. In these missions, radioisotope thermoelectric generators (RTG) are used as power sources, powered by radioactive elements (^{283}Pu, ^{90}Sr). Such devices have successfully been applied in several of space missions like Apollo, Cassini, Pioneer, Viking, and Voyager[8]. The most impressive example is that the power sources of Voyager are in use for more than 25 years, and are still working well.

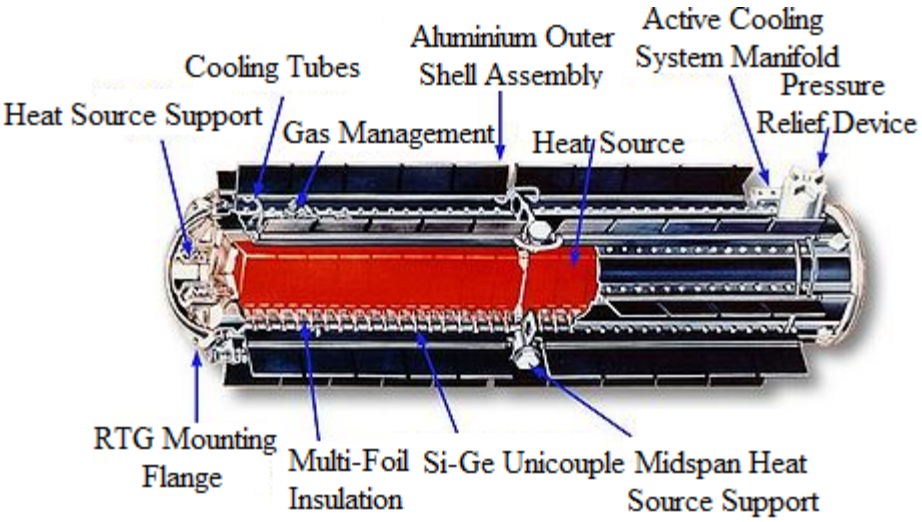

Figure 1.2 Diagram of an RTG used on the Cassini probe[8].

A set up of a thermoelectric power generator is shown in Figure 1.3. Thermoelectric modules consist of both n- and p- type semiconductors. Metal interconnects are used to connect thermoelements with ceramic plates both on the top and at the bottom, used for absorbing heat. When a temperature difference is applied, there will be a potential difference between the two external electrical connections, and then the module can work as a power generator.

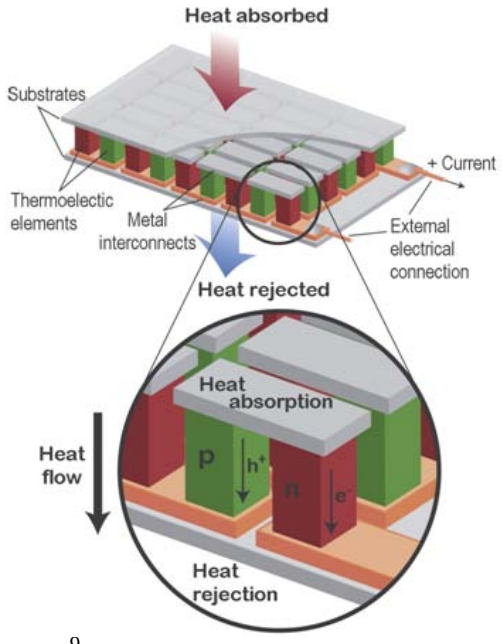

Figure 1.3Thermoelectric module[9].

More than half of the energy generated by human beings is transferred into waste heat. For example, the internal combustion engines of vehicles are highly inefficient in energy use (only 20 - 25% of the energy from fuel combustion can be utilized)[8]. It would be beneficial if it were possible to transform waste heat to reusable energy, such as electricity. Moreover, the new features in modern vehicles such as stability controls, telematics, and navigation systems have heavier usage of electricity[10]. It has been proven that thermoelectric materials are capable of recovering energy from the waste heat of the exhaust gases of automobiles, leading to a reduction in fuel combustion up to 10%, as well as in the production of CO_2. For instance, in the early 1990s, an Automotive Thermoelectric Generator (ATEG) was designed by Hi-Z Inc.[11]. The ATEG is capable of producing 1 kW from a diesel truck exhaust system. The company later also designed ATEG for military vehicles.

Conventional refrigeration technology heavily uses hydrochlorofluorocarbons and chlorofluorocarbons, which are known as ozone depleting substances. Thermoelectric refrigeration applies the 'Peltier' effect to pump heat electronically, and therefore could prevent the emission of ozone-depleting refrigerants into the atmosphere[12,13]. Current international legislation regulates the use of hydrochlorofluorocarbons production. After 2020 in developed countries and 2030 in developing countries, the production of hydrochlorofluorcarbons will be prohibited[5]. Therefore, a great effort has been exerted on developing high efficiency thermoelectric refrigeration devices. Such devices are not only environmental friendly, but also work quietly and require less maintenance. However, comparing with the conventional refrigeration, thermoelectric devices are still low in efficiency.

1.1.3 Applications

The properties of thermoelectric materials allow for varieties of applications. Some successe has been seen in applications like portable refrigerators, beverage coolers, thermopile sensors, RTG, and, more recently, automotive power generation. Due to low efficiency and high cost in comparison with the conventional power generator and refrigerator, commercially available products are limited. A few applications are introduced as follows.

Figure 1.4 shows Hi-Z 14 thermoelectric module and its complete assembly of a 1 kW ATEG for a heavy duty class eight diesel trucks[14]. The module uses bismuth telluride based

materials, targeting the waste heat conversion. It is able to convert 5% of the thermal energy into electricity with a temperature difference of 200°C, and the electrical power output can achieve 14 watts.

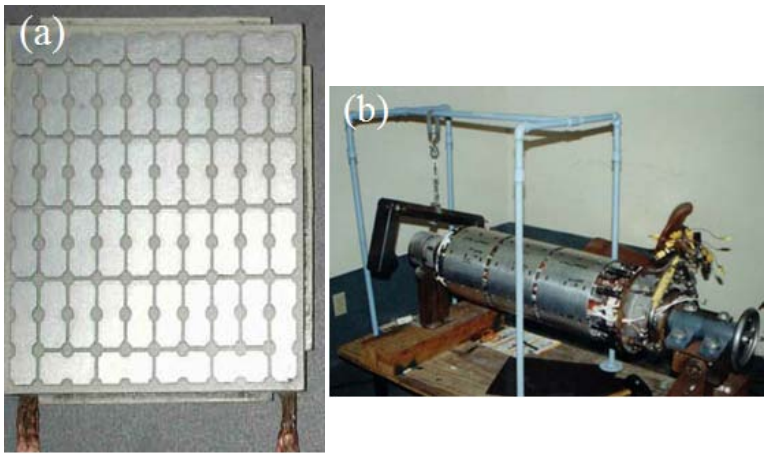

Figure 1.4 (a) Hi-Z 14 thermoelectric module (bismuth-telluride); (b) a complete assembly of ATEG[11, 14, 15].

Peltier devices are almost commonly used for portable refrigerators and for cooling small instruments such as laptops. The thermoelectric cooling module is given in Figure 1.5 (a). Bismuth tellurides are widely used for these cooling devices because they can be suitably doped to have distict ‘n’ and ‘p’ characteristics. A commercially available thermoelectric dual-zone 18 bottle ventilated wine cooler is shown in Figure 1.5 (b). Such coolers use as much energy as a standard light bulb, giving a 150W/110V power output.

Figure 1.5 (a) The thermoelectric cooling module; (b) dual zone thermoelectric wine cooler[16].

1.2 Thermoelectric Properties

The thermoelectric materials in commercial and government applications are rather limited because of their low efficiency. In a power generation device, the efficiency (η) is defined as a dimensionless ratio of energy output to heat energy absorbed at the hot junction[17],

$$\eta = \frac{T_H - T_C}{T_H} \frac{\sqrt{1+ZT}-1}{\sqrt{1+ZT}+T_C/T_H}. \quad [1]$$

Similarly, the performance in a refrigeration mode is a ratio of energy removed to energy expended onto the device[17].

$$\phi = \left(\frac{T_H}{T_H - T_C} \frac{\sqrt{1-ZT}-1}{\sqrt{1+ZT}+1}\right) - \frac{1}{2} \quad [2]$$

The power generation efficiency and coefficient of performance for refrigeration are both related to the Carnot efficiency ($(T_H-T_C)/T_H$) and figure of merit ZT (Table 1.1); T_H and T_C are the temperature at the hot and cold end, respectively. Larger ZT leads to better efficiency in both power generation and refrigeration.

Table 1.1 TE efficiency η in relation with ($T_H - T_C$) and ZT.

ZT	1	1	1	2	2	2	3	3	3
T_H/K	600	900	1200	600	900	1200	600	900	1200
T_C/K	300	300	300	300	300	300	300	300	300
η/%	10.8	15.8	18.7	16.4	23.6	27.7	20.0	28.6	33.3

The figure of merit (ZT) is determined by the following parameters: T, S, σ and κ, that represent the absolute temperature, Seebeck coefficient, electrical conductivity and thermal conductivity, respectively. Since the parameters are interrelated[9], it becomes a great challenge to optimize the parameters to finally achieve high efficiency. From equation [3], high Seebeck coefficient, good electrical conducting property, and low thermal conductivity result in large figure of merit (Figure 1.6).

$$ZT = T\frac{S^2\sigma}{\kappa} \qquad [3]$$

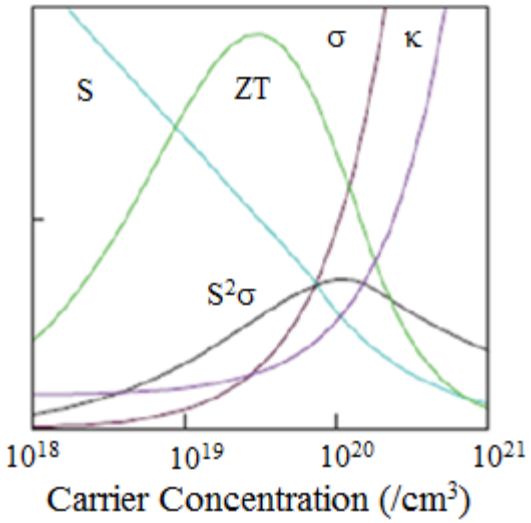

Figure 1.6 Maximizing the efficiency ZT of a thermoelectric material involves a compromise of thermal conductivity (κ), and Seebeck coefficient with electrical conductivity[9].

1.2.1 Carrier Concentration

It is noted that the carrier concentration plays an important role in all three parameters, S, σ and κ. First of all, in a thermoelectric material, positive and negative charge carriers, may co-exist. Mixed electrons and holes lead to a reduction in charge carrier concentration, because both carriers will move toward the cold end, and therefore there will not be electric

potential built up. In equations [5], [6] and [7], n is the carrier concentration, e is the carrier charge (1.602×10^{-19}C), μ is the carrier mobility, κ_e and κ_l are the electronic thermal conductivity and lattice thermal conductivity respectively, and L is the Lorentz factor ($2.44\times10^{-8}J^2K^{-2}C^{-2}$ for free electrons).

$$\sigma = ne\mu \quad [4] \qquad \kappa = \kappa_e + \kappa_l \quad [5] \qquad \kappa_e = L\sigma T = ne\mu LT \quad [6]$$

The electrical conductivity is directly related to charge carrier concentration, and so is the electronic contribution (κ_e) to the total thermal conductivity. For these reasons, semiconductors are best for thermoelectric applications. Although metals conduct electricity very easily, they perform poorly in converting thermal energy to electricity (because of their small Seebeck coefficient). On the other hand, insulators do not have sufficient electrical conductivity. There are only a few elemental semiconductors, however; compound semiconductors can be synthesized, and moreover, the electrical properties of these compounds can be tailored by doping. High carrier concentration is not always favored in improving the ZT value, because the Seebeck coefficient is proportional to $(1/n)^{2/3}$, as shown in equation [7],

$$S = \frac{8\pi^2 k_B^2}{3eh^2} m^* T\left(\frac{\pi}{3n}\right)^{2/3} \quad [7]$$

Another variable that has great impact on the electrical conductivity is the effective mass of the carrier, m^*[9, 18]. The term effective mass of the carrier, m^*, refers to the mass that the carrier seems to carry in the semiclassical model of transport in a crystal. In a crystal, electrons and holes respond to electric and magnetic fields, depending on their travelling direction. When ignoring crystal anisotropies, a free electron in vacuum has a mass of 9.11×10^{-31}kg. The effective mass of the carrier varies in different circumstances, i.e. crystal structures. The effective mass causes another conflict in improving the electrical properties. Large effective mass is beneficial for the Seebeck coefficient (equation [7]), but render the dominant charge carriers less mobile (equation [8])[9]. The mobility is also a function of carrier scattering time (τ), which is high in compounds that consist of elements with close

electronegativity (i.e. carriers can move more freely).

$$\mu = \frac{e\,\tau}{m^*} \qquad [8]$$

Therefore, a balance needs to be found between high effective mass, and the equation [9] derived from Newton`s second law with quantum mechanics indicates that the effective mass is reversely related to the energy dispersion along the wave vector k. However, the mobility (expressed in terms of the velocity of a travelling carrier, v) is positively proportional to the energy dispersion along k[17].

$$\frac{dE}{dk} = \frac{h^2 k}{4\pi^2 m^*} \qquad [9]$$

Large energy dispersion associates with small density of states (DOS), but that causes insufficient charge carrier concentration for conducting electricity. The density of states is also a factor that affects the Seebeck coefficient, but not the only one. The changing derivative of the density of states with energy matters as well[19].

$$S \approx \frac{1}{DOS\,(E)} \cdot \frac{dDOS\,(E)}{dE} \Big|_{E=E_F} \qquad [10]$$

The conflict can be possibly solved by having a large density of states at the Fermi level and a dramatic change in density of states around the Fermi level, and such relationship was described in the equation proposed by Mahan et al., where $\sigma \approx DOS(E_F)$[19,20]. Having a complex crystal structure is essential to obtain such an electronic structure that satisfies all the criteria discussed above.

$$S = \frac{\pi^2}{3} \cdot \frac{k_B^2 T}{e} \cdot \frac{d \ln \sigma(E)}{dE} \Big|_{E=E_F} \qquad [11]$$

1.2.2 Lattice Thermal Conductivity

In a solid, there are two sources for thermal conductivity. When the carriers are

conducting electricity, they are also transferring heat, and this is the electronic contribution discussed before (equation [6]). The other contribution to the total thermal conductivity is the lattice thermal conductivity transported by lattice vibrations (equation [5])[9]. This explains why some materials that are resistive to electricity can still conduct heat, such as diamond and ceramics. Lattice vibrations can be described as atoms vibrating more energetically at one part of a solid transferring that energy to less energetic neighboring atoms. Such motion can be enhanced by a cooperative motion in the form of propagating lattice waves[21].

The phonon contribution to the specific heat in a solid can be estimated by the Debye model which was developed by Peter Debye in 1912. In the Debye model, heat is conducted by the lattice vibrations, and in a defect-free crystal, thermal conductivity should be infinite at all temperatures, if all forces between the atoms are elastic. In another word, the heat conducting will be inhibited if any change happens to these elastic forces between atoms, because the change alters the sound velocity and causes the vibrational waves to scatter. The Debye model only correctly predicts the low temperature dependence of the heat capacity, and recovers the Dulong-Petit law at high temperatures, but it lacks accuracy at intermediate temperatures. Debye's theory on lattice thermal conductivity was improved by Peierls who suggested that the kinetic theory of gasses is valid for vibrational waves (phonons).

$$k_{ph} = \frac{1}{3} C_p \nu l \qquad [12]$$

When the temperature is greater than 300K, the sound velocity and the heat capacity are temperature-independent and therefore the mean free path of phonons is the only factor that influences the lattice thermal contribution. Low lattice thermal conductivity is associated with low bond energies and high atomic masses, because both cause phonons scatter more strongly due to the decreased mean free path. Other factors including atomic disorders and large unit cells can further decrease the mean free path of phonons.

If the walk of energy though the lattice is completely random, a minimum thermal conductivity can be achieved. Such property is usually found in glasses[9, 21]. However, electricity cannot be conducted effectively due to strong electron scattering in glasses. In addition, glasses usually have broad bands, leading to lower effective masses (small density of states). Good thermoelectrics should be able to scatter phonons without significantly affecting

the electrical conductivity. Phonon-glass electron-crystal materials proposed by Slack are ideal for thermoelectric applications[9,22,23]. The substructure approach to separate the electron-crystal and phonon regions is an effective way to achieve coexistence of electron-crystal and phonon-glass (Figure 1.7)[9]. However, since heat transport involves a broad range of phonon, the substructure approach is not sufficient to scatter long-wavelength phonons. Therefore, other approaches such as enhancing complexity are also needed (discussed in later section).

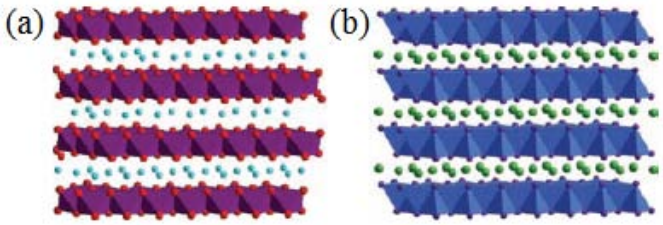

Figure 1.7 (a) Na_xCoO_2 and (b) $Ca_xYb_{1-x}Zn_2Sb_2$ structures both contain ordered layers (polyhedral) separated by disordered cation monolayers, forming coexistence of electron-crystal and phonon-glass[9].

1.3 State-of-Art High ZT Thermoelectrics Materials

Phonon-glass electron-crystal is a strategy to decouple the interrelated parameters. There are a number of materials being researched. Selected thermoelectric materials are reviewed as follows.

1.3.1 Chalcogenides

Chalcogenides refers to sulfides, selenides, and tellurides. These compounds often show semiconducting behavior, which makes them good candidates for thermoelectric materials[9]. The differences in electronegativity between S, Se and Te make it possible to have a large group of different thermoelectric materials, which can be suitable for operation over a wide range of temperatures (200-1400 K)[24]. Nowadays in markets, chalcogenides are the most common thermoelectric materials, such as the famous Bi_2Te_3 and its solid solutions $Bi_2Te_{3-x}Se_x$ and $Bi_{2x}Sb_xTe_3$[25], PbTe, and TAGS (Te-Ag-Ge-Sb)[26].

A ternary compound, $CsBi_4Te_6$ was reported by Kanatzidis et al.. Cesium is introduced into the mixture of bismuth and tellurium, and this results in a new structure type with Bi-Bi bonds[9,27]. Figure 1.8 shows the highly anisotropic layered structure. The slabs of anionic $[Bi_4Te_6]^-$ alternate with layers of Cs^+ ions. Such a complex structure gives a lower lattice thermal conductivity than Bi_2Te_3. In addition to the low lattice thermal conductivity, the decreased band gap due the Bi-Bi bonds (0.08 - 0.1 eV) allows ZT to reach 0.8 below room temperature by doping[27]. Moreover, the layering leads to an anisotropic effective mass, and therefore the Seebeck coefficient can be improved without significantly affecting the mobility.

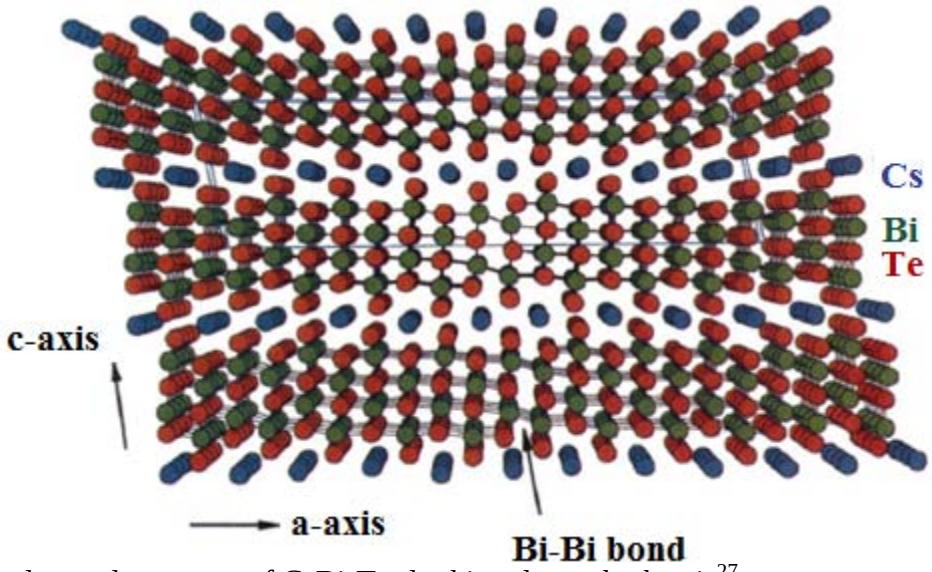

Figure 1.8 The layered structure of $CsBi_4Te_6$ looking down the *b* axis[27].

1.3.2 Skutterudites

The conflicts among thermoelectric parameters are often found in skutterudites containing elements with low electronegativity differences such as $CoSb_3$ and $IrSb_3$. The high degree of covalent bonding, which, as discussed before, allows carriers to move more freely in the crystal, results in good electron-crystal properties[9]. However, the covalent bonding and simple order in the crystal lead to high thermal conductivity. A lot of work has been done on reducing the thermal conductivity of $CoSb_3$ by doping through electron-phonon interactions[28,29].

Filling the large void spaces with rare-earth or other heavy atoms is another solution to the conflict. Effective point-defect scattering can arise by partially filling the void spaces. When the large voids are filled, certain crystallographic orientations which amplify the lattice vibrational modes result, and, therefore, an additional reduction in the thermal conductivity can occur. Filling the void with proper elements can also adjust the carrier concentration. Figure 1.9 (a) indicates the big void spaces in the skutterudites and (b) shows the compound $LaFe_3CoSb_{12}$, where Fe^{2+} (red) ions substitute Co^{3+} (blue), and filled La^{3+} (yellow) is added to fill the void spaces. The ZT value of this compound reaches 1 at 800 K[28]. Recent studies found the possibility to further improve ZT values by partially filling skutterudites, which leads to a favorable combination of low thermal conductivity and higher power factor[29-32].

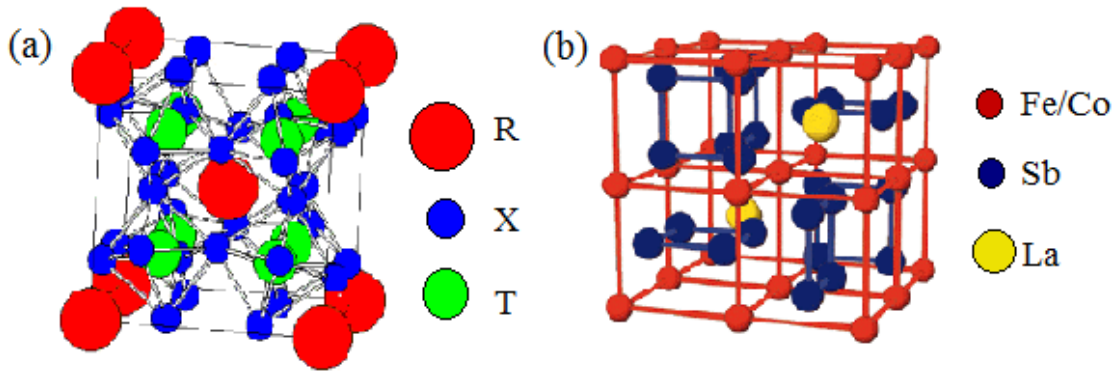

Figure 1.9 (a) A crystal structure of filled skutterudite; (b) a schematic view of a filled skutterudite crystal structure, $LaFe_3CoSb_{12}$[28].

1.3.3 Bulk Materials with Nanocomposites

One effective way to enhance the complexity of the structure and therefore reduce the lattice thermal contribution is to establish distinct regions so that phonon-glass and electron crystal properties can coexist[9]. The two regions having different functions are both beneficial for improving ZT values. The electron-crystal region allows high carrier mobility, while the phonon glass can house the dopants and disordered structures, keeping the carrier mobility uninterrupted. Some nano-materials (e.g. thin films, quantum dots and so on) have demonstrated great thermoelectric properties; nevertheless, materials are required to be produced in large quantities for further commercial applications[33]. Therefore, in that sense, bulk materials with nanocomposites are more beneficial for commercial production.

Recently, a family of so-called LAST materials, lead antimony silver tellurides, $AgPb_mSbTe_{2+m}$, a degenerate semiconductor, was reported to reach ZT = 2.2 at 800 K when m = 15[34]. Transmission electron microscopy (TEM) revealed the existence of various nanodomains concluded to be responsible for the low thermal conductivity of these materials by increasing phonon scattering[35,36]. Theoretical investigation indicated that heat in these semiconductors is mainly carried by acoustic phonons, which are located in a small region in the first Brillouin zone. Nanodomains cause additional boundary scattering, and therefore decrease the phonon mean free path[36]. Hence, when nanodomains occur in a thermoelectric material, phonon propagation will be reduced.

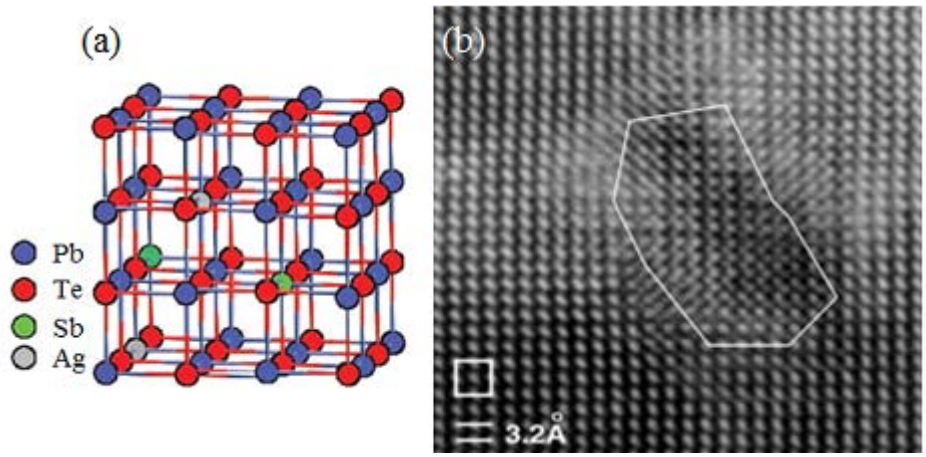

Figure 1.10 (a) Average crystal structure of $AgPb_mMTe_{2+m}$ (m=Sb, Bi) series; (b) TEM image of $AgPb_{18}SbTe_{20}$ sample, showing the separation of Ag-Sb-Te-rich (enclosed area) and Pb-Te rich (surrounding area) regions[33,35].

2. Experimental Methods and Property Measurements

2.1 Synthesis Methods

All samples in this work were prepared in an argon filled glove box, free from oxygen and moisture (Figure 2.1). Because all the starting materials were air and water sensitive, all the reactants were sealed under vacuum after being weighed. The vacuum was provided by Edwards' rotary oil pump (RV5), which can reduce the pressure to the order of 10^3 mbar, measured by Edwards' active gauge controller. There are varieties of solid synthesis methods, and it is difficult to impose a logical order on such a diverse subject. In this work, all samples were prepared by the direct method, which will be introduced in this chapter.

Figure 2.11 An argon filled glove box for sample preparations.

There are a huge variety of methods for preparing solid states materials being developed. Since even with the same composition, materials could be very different in properties depending on how they are prepared. In addition, if a method is too energy and time

consuming, it cannot be used in manufacturing, because the cost will be too expensive. For industrial use, therefore, methods which do not employ extreme conditions (high temperature, high pressure) are favored. For example, diamond requires high pressures during synthesis, but graphite does not[37]. Due to the high cost of synthetic diamond, it is not industrialized. When preparing solids, especially doping thermoelectric materials, it is important to take extra care while using stoichiometric quantities, because properties (e.g. carrier concentration) will be greatly affected. Furthermore, the quality of starting materials is also important to ensure that the right products will be obtained[38,39].

2.1.1 The Direct Method

The direct method is the most basic and most commonly used method of preparing solids. In this method, reactants are usually weighed, mixed by grinding, and heated hard until they react[39]. This method can be applied to synthesize a great number of compounds, including mixed metal oxides, sulfides, nitrides, aluminosilicates and many others[38], so it is widely used for both industry and research purpose. For example, the first high-temperature superconductor was obtained by using the direct method[38]. This solid state synthesis is beneficial for economics, because the elimination of solvents greatly reduces product costs. In a conventional reaction, residual solvents need to be removed to collect the final product, and more purification methods might be required. During such process, the yield of product could be very tiny[40]. The direct method can completely bypass the purification process, and the yield can be improved. Furthermore, no solvent in reactions corresponds to a more environmental friendly process.

Despite of its simplicity and efficiency, the direct method has several disadvantages. In this method, solids are usually prepared at high temperature, typically between 500 and 2000℃, which requires a large energy input. This is because of the high coordination numbers of most compounds, varying from 4 to 12 depending on the size and charge of the ion. In order to leave its position in the lattice and diffuse to a different site, a cation needs a lot of energy to overcome the lattice energy [39]. High temperatures also enhance the mixing of the starting materials. However, a good mixing does not mean the target phase can successfully form. Generally, the solid state reactions usually take place at the interface of the two or more solids, and the reactants continuously diffuse toward the interface (Figure 2.2) and finally

form a homogeneous new phase[39]. In conclusion, high temperature has two purposes: 1) Mixing the reactant to increase reacting interfaces; 2) Speed up the diffusion process. A rule suggests that a temperature of about two-thirds of the melting temperature of the targeted solids gives a sufficient energy for the diffusion. However, diffusion is still the limiting step of the whole reaction. Therefore, starting materials are usually ground to be better mixed (smaller particle size and maximized surface contact area).

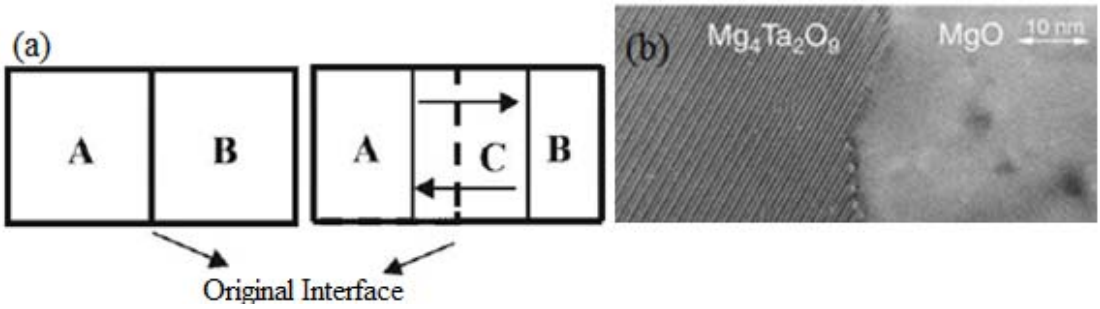

Figure 2.12 (a) Reaction of two components A and B, and more reaction interfaces form during formation of the product layer C; (b) high-resolution transmission electron micrograph showing the reaction front $Mg_4Ta_2O_9$/MgO, formed during the formation of $Mg_4Ta_2O_9$ from Ta_2O_5 and a MgO single crystal at 1100 °C[41].

In solid state, it is not easy to achieve a homogeneous mix of the reactants even after thorough grinding (Figure 2.3). During heating, it might also take infinite time to obtain a pure phase, because diffusion of ions is very slow. Hence, after first heating, products can be collected, ground, pelletized, and annealed again. During the second annealing, fresh surfaces which might be far away from each other in the first heating can be in contact more closely after being reground and pelletized[38]. This procedure can be repeated several times until the targeted compound is obtained without any side products.

Figure 2.13 A pestle and a mortar for fine grinding.

2.1.2 Reaction Vessels

Reaction vessels need to be chosen carefully. They have to be sufficiently inert so that they do not participate in any reaction. They should also be able to withstand high temperature in order to provide a safe environment for reactants. Common reaction vessels are made of silica (to 1430 K), alumina (to 2000 K), zirconia (to 2300 K) or magnesia (to 2700 K)[39]. Depending on the reactions, metals such as platinum, tantalum, and graphite linings are also used in some cases[39]. If the reactants or final products are sensitive to air and water or volatile, an isolated reaction environment is needed. Usually, reaction vessels need to be evacuated and sealed before reactions. In the case of samarium sulfide (SmS) synthesis, sulfur boils at 717K under atmospheric pressure[39]. The reaction is carried out by heating the mixed samarium and sulfur in powdery form at 1000 K. Therefore, a closed evacuated tube (made of either pyrex or silica, depending on the reaction temperature) is required to avoid losing sulfur. An evacuation system with silica reaction tubes connected is shown in Figure 2.4.

Figure 2.14 An evacuation system with (1) silica tubes connected to the vacuum line; (2) a rotary pump providing the vacuum.

2.2 Analysis Methods

2.2.1 X-Ray Diffraction

X-rays were discovered by a German physicist, Wilhelm Röntgen, who was awarded the first Nobel Prize in Physics in 1901 for this discovery. X-rays have been applied in medical diagnosis and treatment, and in investigating molecular and atomic structures. The benefits brought by its discovery are immeasurable.

X-radiations are emitted by electrons outside the nucleus, having a wavelength in the range of 0.1 Å to 100 Å (Figure 2.5), the same order as the bond lengths between atoms in crystals (1 - 4 Å). Since X-rays can penetrate solid objects, one of the uses is to take images of the inside of objects in diagnostic radiography and crystallography.

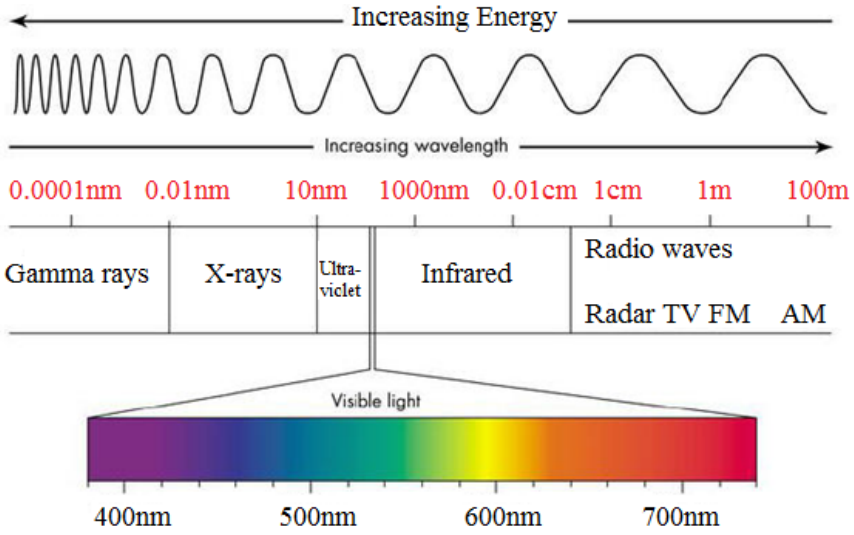

Figure 2.15 The electromagnetic spectrum.

An X-ray tube (Figure 2.6) is composed of a tungsten filament (cathode), which is separated by about 1 cm from the metal target (anode) in an evacuated glass (very high vacuum). The metal target can be Cu, Mo, etc[42]. Electrons emitted from an electrically heated filament are accelerated by passing by a high potential difference (20 – 50 kV). These electrons with high speed strike the metal target, and around 2% of the electrons produce X-rays, while the rest create heat only[42]. To avoid the melting of the metal target, it must be cooled by a water flow.

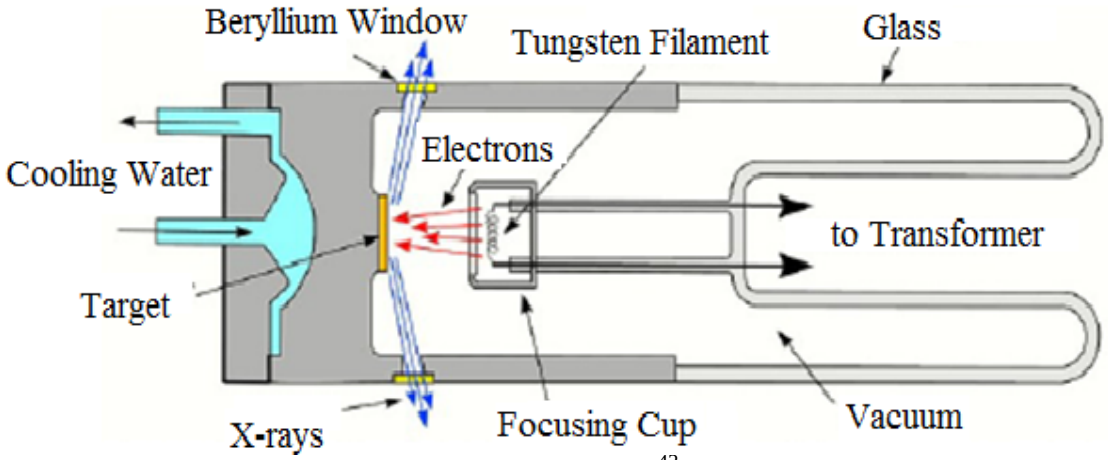

Figure 2.16 A schematic cross section of an X-ray tube[43].

X-rays emitted are not monochromatic, but instead they cover both white radiations and other characteristic radiations including K_α and K_β lines. For X-ray diffraction, monochromatic radiation is very important. This can be achieved by using proper filters or a single crystal monochromator. The frequencies of the K_α and K_β lines are characteristic of the metal target (Figure 2.7). The bombarding electrons knock out electrons from the intermost K shell, and vacancies created are then filled by the electrons descending from the L shell. The energy lost by the descending electrons appears as radiation[44]. Similarly, K_β lines correspond to M to L shell transition. Copper and molybdenum have K_α lines at 1.5419 Å and 0.7101 Å, respectively[42]. Filters can be selected depending on the type of the target metals (Table 2.1). Usually, the filter is made of a thin metal foil of the element adjacent (Z−1) to the target metal in the Periodic Table; thus, nickel can effectively absorbs the K_β line of copper[45]. A monochromatic beam of X-rays can also be selected by reflecting the X-ray beam from a plane of a single crystal, such as graphite, quartz, germanium, LiF, etc[45]. The single crystal is placed in an accurate orientation to the X-ray beam in such a way that only K_α can interfere constructively.

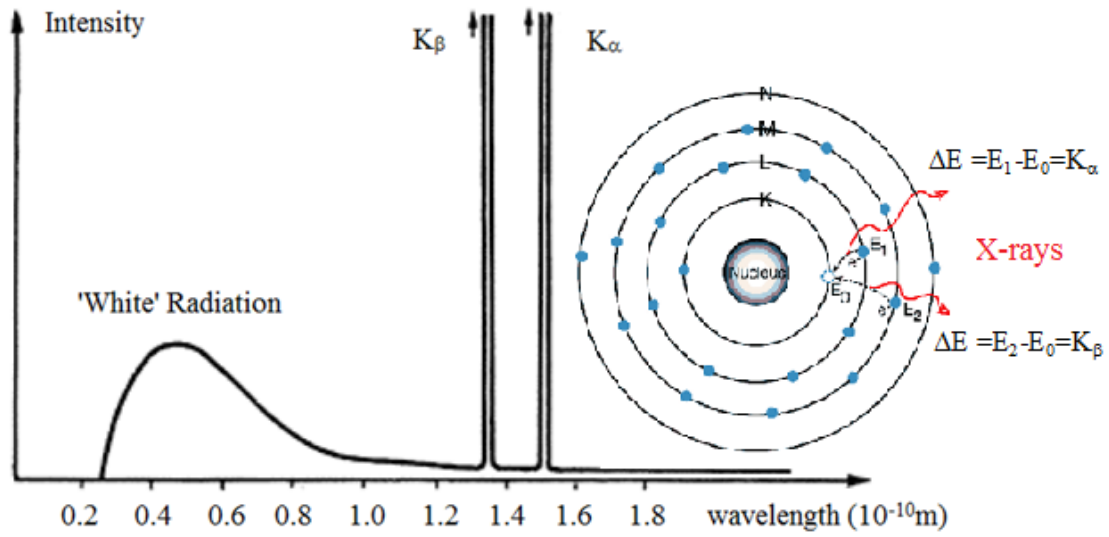

Figure 2.17 X-ray emission spectrum of a metal, e.g. Cu, showing the generation of K_α and K_β rays[44].

Table 2.2 Filters for common metal targets[44].

Metal Target (Z)	Emitted Lines	Wavelength (Å) $K_{\alpha1}/K_{\alpha2}/K_\beta$	Filter(Z)	Wavelength (Å)
Mo(42)	$K_{\alpha1}/K_{\alpha2}/K_\beta$	0.7093/0.7135/0.6323	Zr(40)	0.6888
Cu(29)	$K_{\alpha1}/K_{\alpha2}/K_\beta$	1.5405/1.5443/1.3922	Ni(28)	1.4869
Co(27)	$K_{\alpha1}/K_{\alpha2}/K_\beta$	1.7889/1.7928/1.6207	Fe(26)	1.7429
Fe(26)	$K_{\alpha1}/K_{\alpha2}/K_\beta$	1.9360/1.9400/1.7565	Mn(25)	1.8954
Cr(24)	$K_{\alpha1}/K_{\alpha2}/K_\beta$	2.2896/2.2935/2.0848	V(23)	2.2676

2.2.2 Reaction Vessels

The wave nature of X-ray diffraction was not resolved until1912. Two years later, Max von Laue earned the Nobel Prize for his work on demonstrating the wave nature of X-ray diffraction effects[46]. This was achieved by using a crystal of copper sulfate as the diffraction grating. Crystalline solids have layered structures. Each layer can be considered as a regular array of atoms, ions or molecules with interatomic spacings of the order of 100 pm. X-ray diffraction can take place because the wavelength of the incident light is of the order of magnitude as the spacings. A crystal can work as a three-dimensional diffraction grating to X-

rays due to the periodic nature of the structure. Soon after this discovery, W. H. and W. L. Bragg (father and son) started experiments on using X-ray diffraction for structural analysis. It was noted that X-ray diffraction reflects from the layers of atoms, but it happens only at specific orientations of the crystal with respect to the incident beam and the detecting device[46]. The reflection only occurs when the conditions for constructive interference are fulfilled (the Bragg condition), and this is different from the reflection of light from a mirror, which requires that the angle of incident beam equals the angle of reflection, possible for all angles. Bragg determined many structures including NaCl, KCl, ZnS, CaF_2, $CaCO_3$ and diamond[46].

Figure 2.8 demonstrates how the reflection of X-rays by a crystal satisfies Bragg's condition. Each line connected by the black dots represents a section through the crystal. In order to satisfy Bragg's condition, parallel incident rays, which are in phase, are taken into account. The top incident beam A strikes the atom at B, and the second beam D continues to the next layer where it is scattered by another atom F. The second beam travels an extra distance, called difference in path length, EF+FG, before detected. The path lengths of the two beams differ by an integer number of wavelengths (in phase), having the following relationship[46]:

$$EF + FG = n\lambda = d\sin\theta \qquad [1]$$

The equation is known as the Bragg equation, in which d and θ represent the spacing between the crystal planes and the angle of incident beam, respectively.

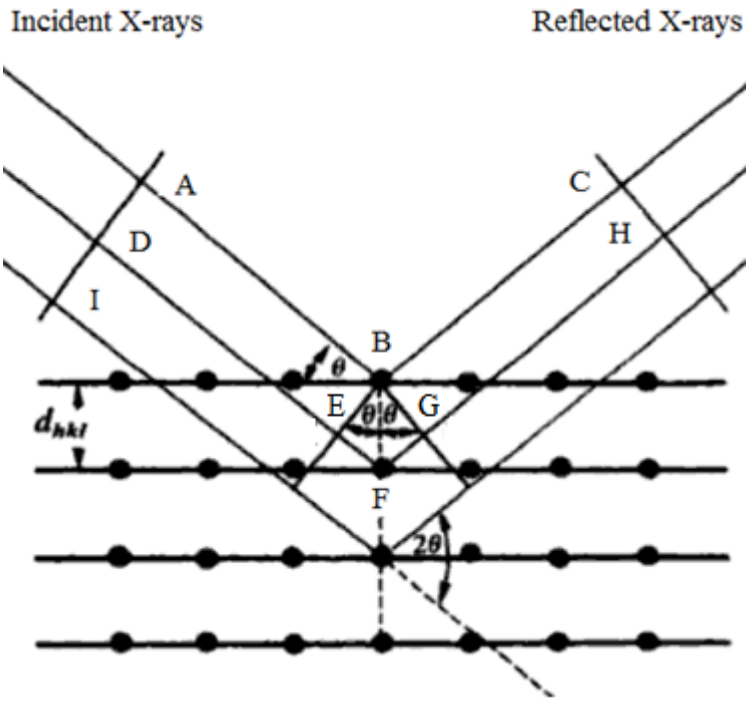

Figure 2.18 Derivation of Bragg's law for X-ray diffraction[46].

A sample with random orientation of crystals between 0.1 and 10 micron is sufficiently fine for taking a powder X-ray diffraction pattern. When an X-ray beam strikes this polycrystalline sample, the beam is scattered in all possible directions, with each plane of atoms separated by different lattice spacing in the crystal leading to cones of diffraction[47]. The diffraction is usually described in reciprocal space by the Ewald sphere, a sphere with radius $1/\lambda$ that starts at the origin of the reciprocal space. For each reciprocal lattice point that is located on this sphere, Bragg's law is satisfied and diffraction is observed[46].

The graphical representation (Figure 2.9) on the Ewald sphere shows the structural information in the reciprocal space (it shows 1/d instead of d spacing directly)[48]. Each orientation of the crystal with respect to the incident beam that obeys Bragg's law is transformed to a single point[47]. One constructs vectors from an arbitrary origin perpendicular to each family of planes with lengths equal to the reciprocal of the d-spacing of each family. It generates a new lattice in a space with linear dimension of the reciprocal of length. The length coordinates in this discrete reciprocal space are h, k, and l, and the coordinate axes are designated a^*, b^* and c^*. The reciprocal lattice has dimensions that are reciprocal to the direct lattice, and its size corresponds to the inverse of the unit cell. The intensities I(hkL) in reciprocal space are proportional to the squares of the crystallographic structure factors,

F(hkl)[49]. The structure factor is expressed as in equation [2], where f_j is the atomic scattering factor for atom j, h, k, l are the miller indices and x, y, z are the relative atomic positions in the unit cell. Other than F(hkl) [2], the phase of the structure factor is also needed to perform crystal structure determination, and it is related to the electron density, which can be obtained from an X-ray diffraction pattern[49]. The 3-dimensional intensities in reciprocal space of polycrystalline samples are compressed into a 1-dimensional pattern. The pattern consists of peak positions, intensities and shapes of Bragg`s reflections, which are affected by 1) space group; 2) unit cell dimensions; and 3) types of atoms and the corresponding coordinates in the unit cell. Unit cell dimensions affects the peak positions, coordinates and scattering factors influence peak intensities, and crystallinity, disorders and defects change peak shapes[49]. In equation [2] - [5], (x_j, y_j, z_j) are the coordinates of an atom in the crystal unit cell.

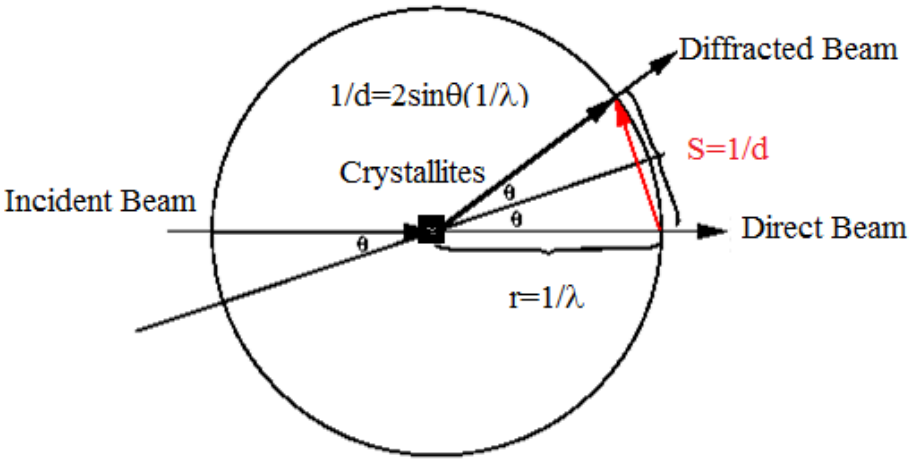

Figure 2.19 Ewald sphere and Bragg's law in reciprocal space[46].

$$F(hkl) = \sum f_j \exp\left[2\pi i(hx_j + ky_j + lz_j)\right] \quad [2]$$

$$F(hkl) = \sum f_j \{\cos\left[2\pi(hx_j + ky_j + lz_j)\right] + i\sin\left[2\pi(hx_j + ky_j + lz_j)\right]\} \quad [3]$$

$$F(hkl) = |F(hkl|\exp(i\phi) \quad [4]$$

$$I(hkl) \propto F(hkl)^2 \quad [5]$$

A detector is another important part of any diffraction analysis system and it measures the position and intensity of diffracted beams. Different types of detectors exist, such as CCD

(charge coupled devices, Figure 2.10), PSD (position sensitive detectors), and IPD (image plate detectors)[50]. Collection of powder diffraction patterns is now almost always performed by the former two, which have better resolution. The position and intensity can be readily self-measured and stored on a computer for future analysis. The experimental results presented here were obtained by utilizing the INEL powder diffractometer with position-sensitive detector and Cu K_α radiation. Single crystal analysis is another important technique based on X-ray diffraction, but it will not be introduced because it was not applied in here.

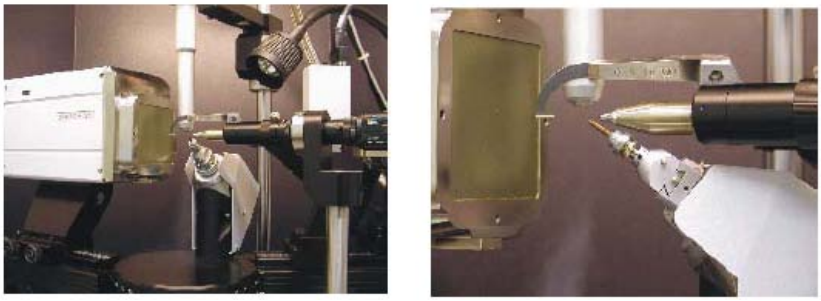

Figure 2.20 Bruker Smart APEX CCD and four-circle diffractormeter.

2.2.3 The Rietveld and Le Bail Methods

X-ray diffraction of powder samples results in a pattern characterised by peaks in intensity at certain position. The height, width and position of these peaks can be used to determine many aspects of the materials structure. However in powder diffraction technique, the compression of a 3-D diffraction pattern into 1-D can lead to overlapping peaks and information loss. On the other hand, it may be difficult to have a single crystal with good quality that can be used for the single crystal analysis.

Full pattern methods are very powerful in solving crystal structures in determination of unit cell parameters, and they fall into two categories, the Rietveld method and the Le Bail method[51]. The Rietveld method involves the computation of reflection intensities from a solved structural model. It uses a least squares approach to refine a theoretical line profile until it matches the measured data[51]. The Le Bail is usually used to apply full pattern methods when structural information is unknown or limited. In this thesis, the Le Bail method was preferentially used to obtain lattice parameters, because the disorder caused by adjacent atoms (Tl, Pb, Bi) in the Periodic Table cannot be solved by the current techniques.

The Le Bail method is also called the whole-powder pattern decomposition method. In this method, the reflection positions are still calculated from the space group and initial unit

cell parameters, but the intensities are considered as arbitrary unknowns.The refined result is used to generate a pattern which matches the experimental data the best. By refining lattice dimensions and other parameters, the intensities evolve iteratively. Other parameters include background function, peak profile, and instrument zero[51]. The algorithm of the Le Bail method has been implemented as an option in some Rietveld programs. The computer program for structural analysis and refinement used in this thesis is GSAS (General Structure Analysis System)[52].

2.3 Physical Property Measurements and Characterization Methods

Physical properties need to be measured to examine the performance of the materials. The parameters, including the Seebeck coefficient, electrical conductivity, and thermal conductivity, can then be determined to calculate the dimensionless figure of merit, ZT, which indicates whether the materials are qualified for thermoelectric applications in the future. The measurements require accuracy and consistency in order to successfully characterize the materials. All property measurements were carried out at University of Waterloo. Both cold and hot pressed samples were used. The cold pressed samples were prepared and annealed before measurements in University of Waterloo. The hot pressed samples were prepared in University of Stookholm by Dr. M. Nygren by using SPS technique (Spark Plasma Sintering)[53]. Densities of the samples were calculated from the weights and dimensions measured by a balance and caliper respectively.

2.3.2 Electrical Conductivity and Seebeck Coefficient Measurements

Electrical conductivity and Seebeck coefficient measurements were both carried out simultaneously by using ULVAC ZEM-3 system. The instrument allows measurement of both 6 to 22 mm long prism and cylindrical samples. Before starting the measurement, a V-I plot can be easily and quickly made to check whether the sample is properly contacted with the detecting probes. The temperature range can be preset by using a computer, all measurements can be controlled by the computer, and raw data are automatically saved.

Figure 2.21 ULVAC ZEM-3 Seebeck coefficient/electrical resistance measuring system[54].

The resistivity is measured by using the four-terminal sensing method (also called 4-wire sensing, or 4-point probe method, Figure 2.11). It is an electrical impedance measuring technique which applies separate pairs of current-carrying and voltage-sensing electrodes to make more accurate measurements than traditional two terminals (T). A current is supplied via a pair of force connections (the outer two contacts in Figure 2.11). Usually, the resistance of the connecting wires and the contacts is small enough to be neglected, especially when measuring a very resistive sample[55]. But if the connecting wires are long, or the sample has very small resistance, those resistances are not irrelevant anymore.

Both two-point and four-point probe methods are demonstrated in Figure 2.11. Figure 2.11 (a) shows how the total resistance R_T is measured,

$$R_T = R_W + R_C + R \qquad [6]$$

where R_W, R_C and R are the resistance of the connecting wires, contacts and sample respectively. Apparently, it is not possible to determine R from the measured R_T. The current path in the four-probe method (Figure 2.11 (b)) is the same as in Figure 2.11 (a), but the voltage is measured by using two additional contacts. Although the new path also contains R_W' and R_C', the whole measurement can be greatly improved. This is because R_W' and R_C' in the new path are negligible due to the high input impedance of the voltmeter (10^{12} Ω or higher)[55].

The fine powdery sample is pressed into a bar shape pellet, and the pellet is attached by

four probes. When a power is applied, a current (I) passes through the sample. The voltage, V, will be measured at the two middle contacts. The electrical conductivity, σ, is calculated from the resistance,

$$\sigma = 1/\rho \qquad [7] \qquad\qquad \rho = R \times A/L \qquad [8]$$

where ρ is the resistivity, A is the area of the cross section of the sample, and L is the distance between the middle two probes.

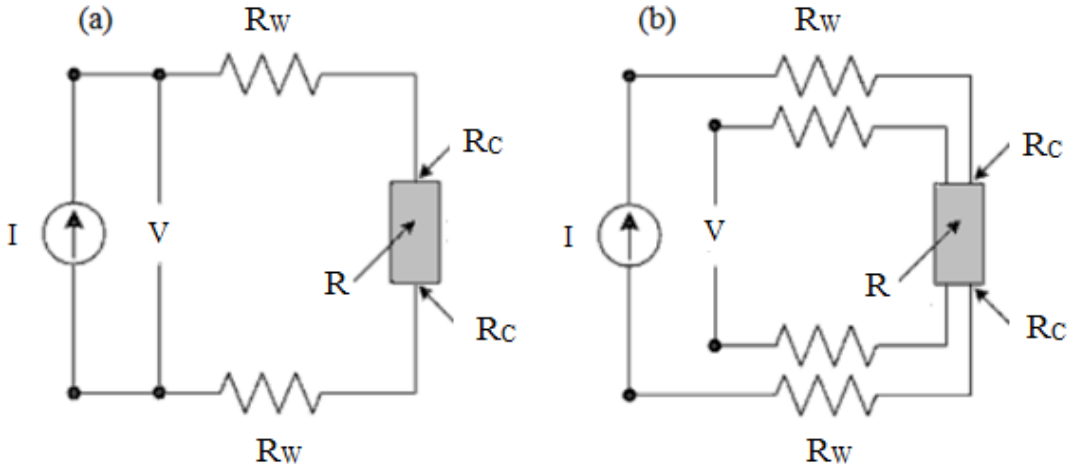

Figure 2.22 (a) Two-terminal and (b) four-terminal resistance measurement arrangements[55].

The Seebeck coefficient is defined as the ratio of the voltage difference to the temperature difference between two sides of the materials ($S = \Delta V/\Delta T$). The Seebeck coefficient presented in this thesis was measured together with the electrical conductivity by ULVAC ZEM-3 based on the slope of a voltage versus temperature-difference curve.

2.3.3 Thermal Conductivity Measurements

Thermal conductivity is the ability of a material to conduct heat, and can be calculated from Equation [8],

$$\kappa = \alpha \rho C_p \quad [8]$$

where α is the thermal diffusivity, ρ is the density, and C_p is the specific heat of the material[56]. While the density is known, the unknown parameters, α and C_p, will be determined by the flash method and C_p can be derived from the Dulong-Petit law.

The thermal diffusivity of a material describes the speed of heat propagation through the material, and it contains information that is essential to evaluate the heat flow and temperature variations in materials under temperature gradients and to understand their thermal performance. The laser flash technique is the most prominent and preferred method nowadays, developed in the U. S. radiological defence by G. L. Abbot[56], because of its several advantages. It does not require long measurement time or large sample size. It can measure thermal diffusivity over a wide range of temperatures and be operated easily. In this method, a pulse of laser radiation is generated to strike the front surface of a thin sample which is controlled at a predetermined temperature by accurately monitoring transient temperature variations to the rear surface of the sample. The temperature T(L, t) at the rear surface of the sample at any time can be expressed by[56],

$$T(L,t) = \frac{Q}{\rho C_p L}\left[1 + 2\sum_{n=1}^{\infty}(-1)^n \exp\left\{\frac{-n^2\pi^2\alpha t}{L^2}\right\}\right] \quad [9]$$

where Q is the energy absorbed on the front surface from the laser pulse. The maximum temperature can reach:

$$T_{L(max)} = \frac{Q}{\rho C_p L} \quad [10]$$

The ratio of $T(L, t)/T_{L(max)}$ varies between 0 and 1, and can be plotted as a function of t/t_c, where t_c is $L^2/(\pi^2\alpha)$, a function of thermal diffusivity (Figure 2.12). When there is no heat loss (A), the maximum temperature change can be observed, otherwise, curves like B or C are be detected[57]. At $t_{1/2}$, the half time that it takes to reach ΔT_{max}, $t_{1/2}/t_c$=0.137, so, therefore, the thermal diffusivity can be calculated from the measured half time[58]. The equation was originally proposed by Parker, assuming the sample is isotropic and adiabatic.

$$\alpha = 0.1388\frac{L^2}{t_{1/2}} \qquad [11]$$

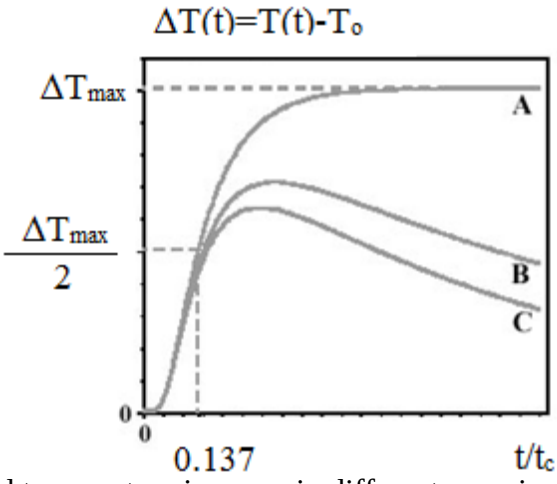

Figure 2.23 The observed temperature increase in different experimental conditions[57].

The thermal diffusivity presented in the thesis was measured by the FlashLine 3000 thermal diffusivity system from ANTER Corporation (Figure 2.13 and 14), and the flash was generated from a Xenon lamp.

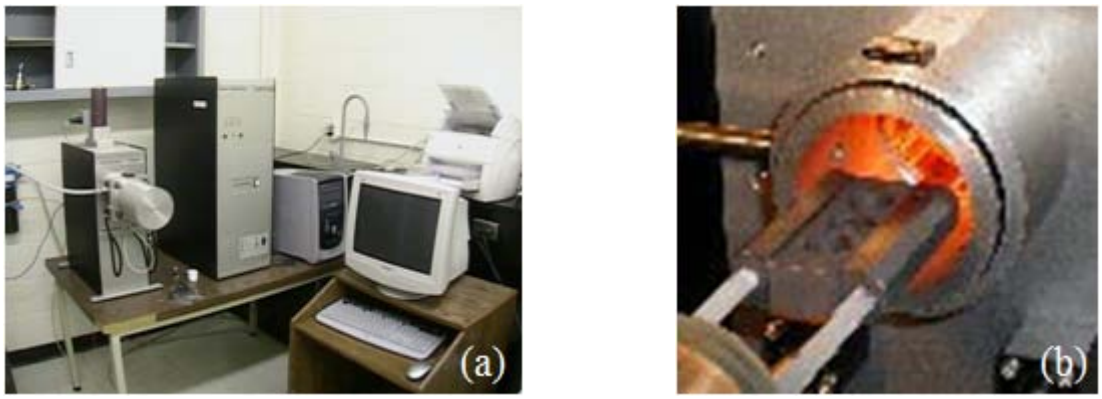

Figure 2.24 (a) The FlashLine 3000 device; (b) the sample holder.

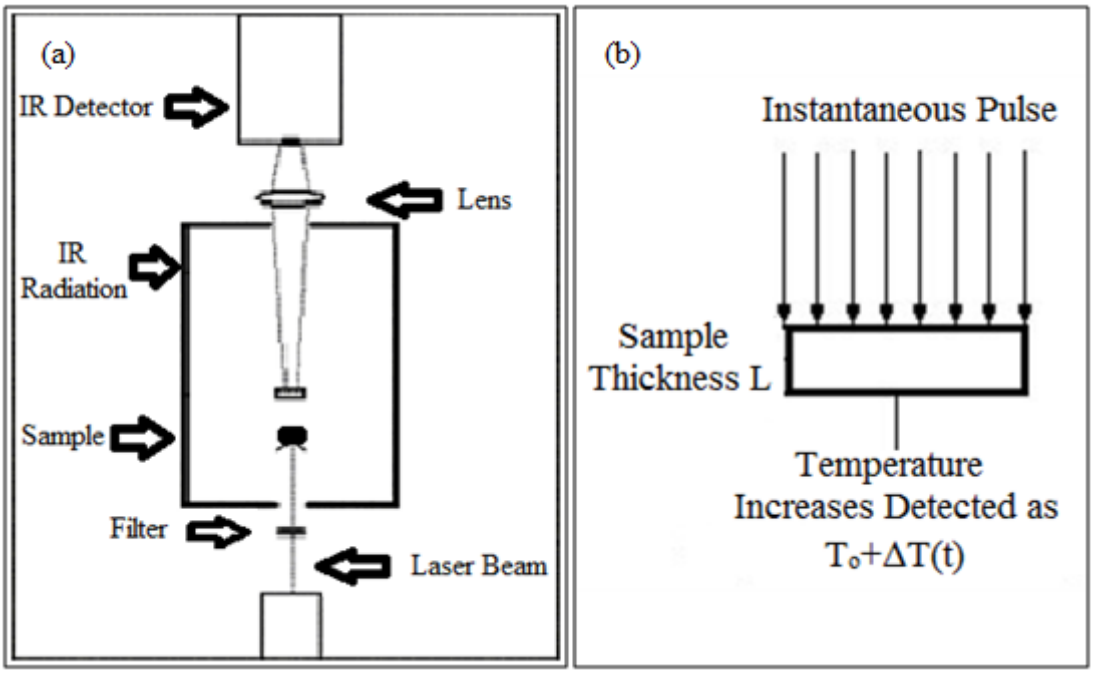

Figure 2.25 (a) The cross section of the FlashLine 3000 device; and (b) the pulse shooting the sample in the flash method.

The specific heat of a material at high temperature can be calculated based on the Dulong-Petit law, proposed in 1819 by French physicists and chemists Pierre Louis Dulong and Alexis Therese Petit[59]. The law states the classical expression for the specific heat capacity of a crystal due to the lattice vibrations. The two scientists measured the values of heat capacities multiplied by atomic weights, which were determined to be almost constant[59]. They further offered a good prediction for the specific heat capacity of solids at high temperatures. According to the Dulong-Petit law, the specific heat, C_p can be calculated at high temperatures[59],

$$C_p = 3R/M_M \quad [11]$$

with R being the natural gas constant, and M_M the molar mass per atom.

3. Ternary Tellurides

3.1 Introduction

Tetradymite-like layered ternary compounds in the systems $A^{IV}B^{VI}$-$A^{V}{}_2B^{VI}{}_3$ (A^{IV} = Ge, Sn, Pb; A^{V} = Bi, Sb; B^{IV} = Se, Te) exhibit outstanding thermoelectric properties due to their complex crystal structures[60-65]. Long period multilayer structures lead to lower lattice thermal conductivity in comparison with other tellurides (Table 3.1 and Figure 3.1). Ternary lead bismuth tellurides, consisting of the heaviest group 15 and 16 elements, were studied. Oosawa's group reported that $PbBi_2Te_4$ and $PbBi_4Te_7$ have excellent thermoelectric properties[65]. However, the phase range of the system remains contradictory, and $PbBi_4Te_7$ has not been obtained pure so far[66-69]. Hence, a phase range study for the system is required not only to know more details about the existing phases, but also to explore the potential for doping work in the future.

First of all, it is necessary to clearly identify the existing compounds in the system. Elagina and Abrikosov reported the only ternary compound was $PbBi_4Te_7$, which forms peritectically at 850 K[66]. Golovanova et al. agreed that $PbBi_4Te_7$ is the only compound but that it melts congruently[67]. Two compounds $PbBi_2Te_4$ and $PbBi_4Te_7$ were identified by Chami et al., and they were also reported to form peritectically at 843 K and 856 K respectively[69]. Nevertheless, Skoropanov et al. believed that $PbBi_2Te_4$ melts congruently[70]. The system has a very slow equilibration, which may cause the above discrepancies[71].

The unit cells and crystal structure are shown in Table 3.1 and Figure 3.1. The X-ray diffraction patterns of $PbBi_2Te_4$, $PbBi_4Te_7$ and $PbBi_9Te_{10}$ (Figure 3.2 - 3.4) are very similar and the only distinct peaks appear at 19.23[72], 18.57[71], and 18.17[70], respectively (Table 3.2).

Table 3.1 Structural information of $PbBi_2Te_4$[72] and $PbBi_4Te_7$[71] from a previous study.

Compound	Space Group	Lattice Dimension	Structural Description
$PbBi_2Te_4$	$R\bar{3}m$	a = 4.452(4) Å c =41.531(4) Å	a 12-layer structure
$PbBi_4Te_7$	$P\bar{3}m1$	a = 4.426(1) Å c = 23.892(2) Å	a 21-layer structure

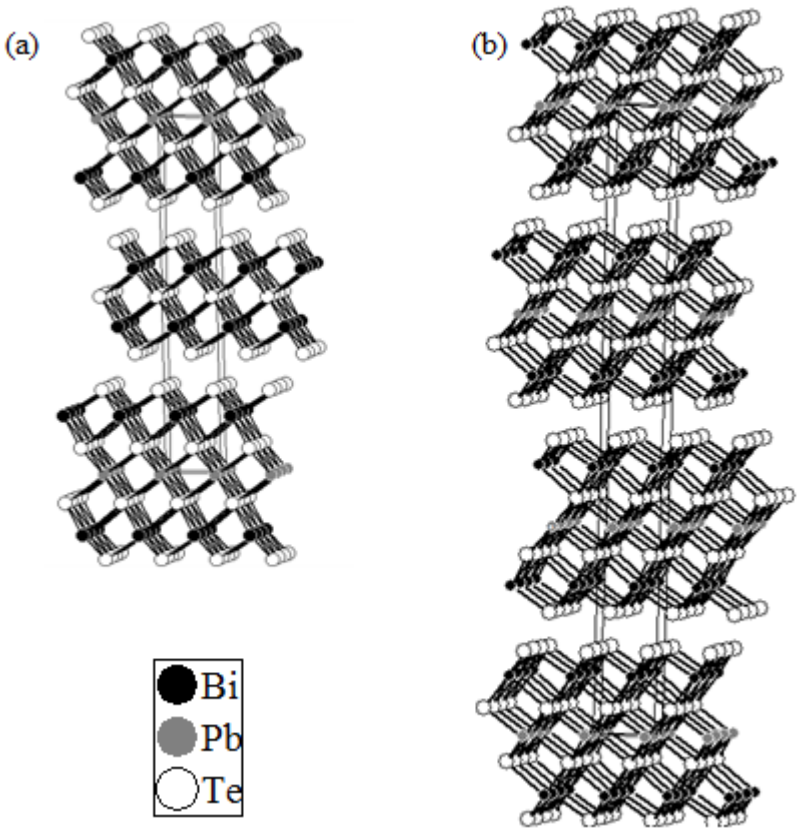

Figure 3.1 Crystal structures of (a) $PbBi_2Te_4$, and (b) $PbBi_4Te_7$, viewed along [100], assuming each layer is homogenously occupied by only one element.

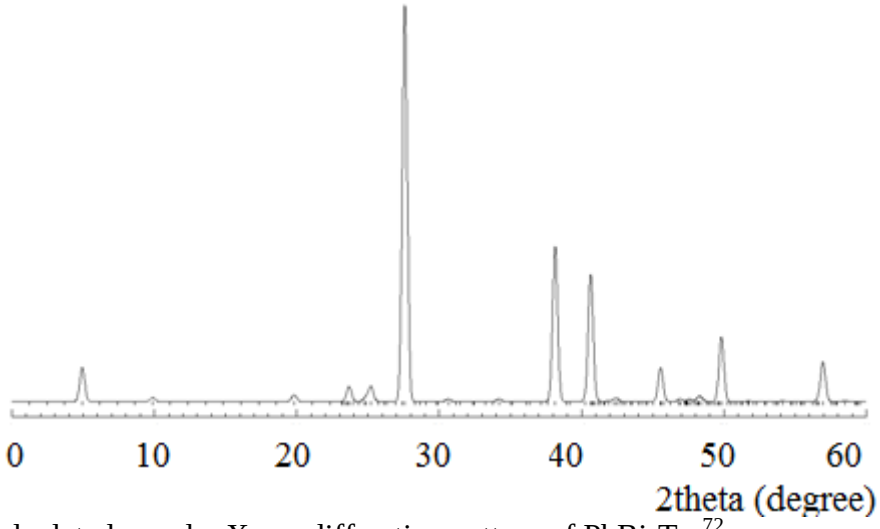

Figure 3.2 Calculated powder X-ray diffraction pattern of $PbBi_2Te_4$[72].

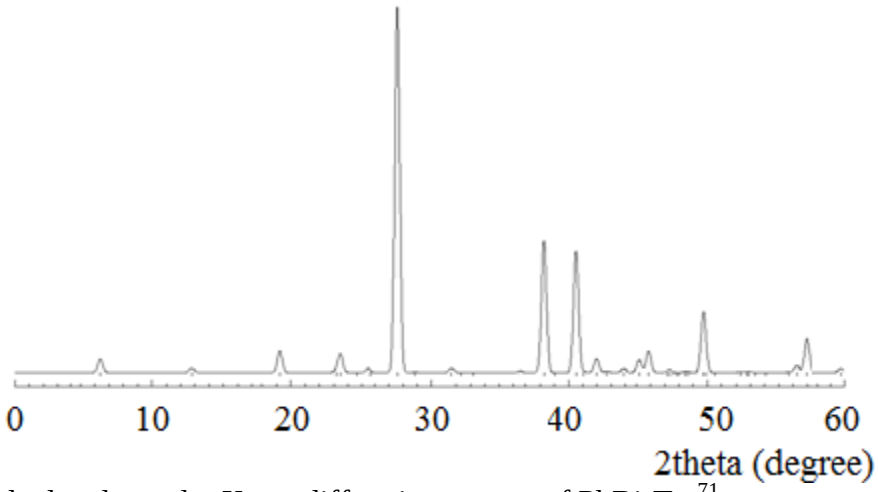

Figure 3.3 Calculated powder X-ray diffraction pattern of $PbBi_4Te_7$[71].

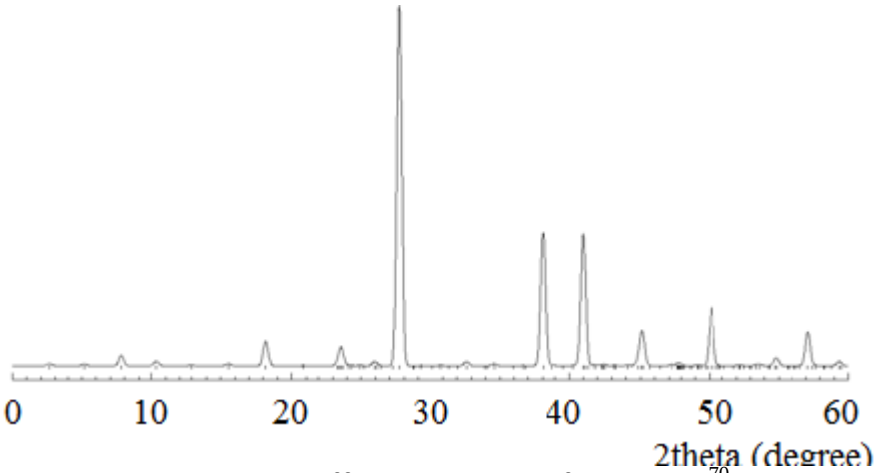

Figure 3.4 Calculated powder X-ray diffraction pattern of $PbBi_6Te_{10}$[70].

Table 3.2 Major distinctions among $PbBi_2Te_4$, $PbBi_4Te_7$ and $PbBi_6Te_{10}$.

Compound	2 theta (degree)
$PbBi_2Te_4$	19.23
$PbBi_4Te_7$	18.57
$PbBi_6Te_{10}$	18.17

Previous solutions to the structures of $PbBi_2Te_4$ and $PbBi_4Te_7$ are listed in Table 3.3 and Table 3.4, respectively. These published results can only be considered as the best guesses at the real structures so far. In 1972, T. B. Zhukova and A. I. Zaslavskii indicated that Pb atoms and Bi atoms both occupy 3a, but with occupancies of 0.333 and 0.667 respectively, and the same mixed occupancy also happens at 6c[72]. In 2004, Shelimova et al. described the structure of $PbBi_4Te_7$ in such way that there are no mixed occupancies in the unit cell[71]. Since the

scattering coefficients of Pb and Bi atoms are very similar, in X-ray diffraction patterns of $PbBi_2Te_4$ and $PbBi_4Te_7$, peaks contributed by Pb and Bi are not distinguishable. Hence the sequences of each layer in Figure 3.1 are estimated by assuming that the systems are cooled in a certain rate that such ordering can occur. The reality is that Pb and Bi can have any kind of ordering within one compound greatly depending on how the compound is prepared. If Pb and Bi occupy the black and grey layer in Figure 3.1 completely randomly, the local structure will be much more complex. Such complexity has the advantage of leading to low thermal conductivity, but a good strategy to study the system to obtain consistent results is the only way to solve the puzzle.

Table 3.3 Detailed structural information of $PbBi_2Te_4$[72] from a previous study.

Atom	Atom Site (x, y, z)	Wyckoff Position	Occupancy
Pb^{2+}	0 0 0	3a	0.333
Bi^{3+}	0 0 0	3a	0.667
Pb^{2+}	0 0 0.4285	6c	0.333
Bi^{3+}	0 0 0.4285	6c	0.667
Te	0 0 0.136	6c	1
Te	0 0 0.289	6c	1

Table 3.4 Detailed structural information of $PbBi_4Te_7$[71] from previous study.

Atom	Atom Site (x, y, z)	Wyckoff Position	Occupancy
Pb^{2+}	0 0 0	1a	1
Bi^{3+}	0.3333 0.6667 0.8329	2d	1
Bi^{3+}	0.3333 0.6667 0.5840	2d	1
Te^{2-}	0.3333 0.6667 0.0781	2d	1
Te^{2-}	0 0 0.2369	2c	1
Te^{2-}	0.3333 0.6667 0.3439	2d	1

From the previous studies, there are three major problems; 1. determining the existing compounds in the system; 2. confirming the structures of the existing compounds using X-ray diffraction patterns; 3. constructing a correct phase diagram of the systems. For finding good thermoelectric materials, the three major problems can be modified as follows, 1. determining the stable compounds in the system; 2. successfully reproducing the good thermoelectric materials among these stable compounds; and 3. collecting more structural information on these compounds. It is very easy to understand that unstable compounds even with ‘good’

thermoelectric properties do not have manufacturability. Secondly, if it costs too much for a material to be reproducible, no investor would be interested in such materials. Furthermore, the structural analysis is essential for us to understand the properties of the materials and for us to construct reasonable computational simulations. To start with, the listed reactions in Table 3.5 were carried out, and detailed synthesis, final products, structural analysis, and physical properties are discussed in the following sections.

Table 3.5 Targeted stoichiometry.

Stoichiometry Pb:Bi:Te	Estimated Charge Carrier (cm^{-3})
1:2:4	0
0.7:2.3:4	$-1x10^{21}$
0.9:2.1:4	$-4x10^{20}$
1.1:1.9:4	$4x10^{20}$
1.3:1.7:4	$1x10^{21}$
0.85:4.15:7	$-4x10^{20}$
1:4:7	0
1.15:3.85:7	$4x10^{20}$
1.35:3.65:7	$9x10^{20}$

3.2 Synthesis and structural Analysis

All reactions were started from elements with high purity (Pb, granules, -3 mm, 99.99%, Alfa Aeasar; Bi, powder, -100 mesh, 99.5%, Alfa Aesar, Te, granules, -3mm to +50 mesh, 99.99%, Alfa Aesar). Samples were weighed and mixed in an argon-filled glove box according to the expected chemical formula. The total amount was around 3 grams for each sample. Silica tubes were used as reaction vessels, which were sealed under vacuum after weighing. The tubes were then heated and cooled in a certain rate (Table 3.5). The products were crushed and pulverized, and pellets were made by using a mechanical die in a hydraulic press. The pellets were sealed in silica tubes under vacuum and annealed at 848 K for 45 days. The tubes were slowly cooled in 48 hours, and samples were crushed and ready for analysis. Two samples $Pb_{0.8}Bi_{2.2}Te_4$ and $Pb_{0.9}Bi_{2.1}Te_4$.were found to be pure after powder X-ray diffraction analysis. Le Bail refinements were performed for $Pb_{0.8}Bi_{2.2}Te_4$ and $Pb_{0.9}Bi_{2.1}Te_4$ to calculate cell dimensions. Pure samples were pressed into rectangular and cylindrical pellets for physical property measurements. The cold pressed samples achieved 80% of the theoretical densities.

Table 3.6 Reaction conditions and corresponding products.

Stoichiometry Pb:Bi:Te	Intermediate Product	Equilibrium Product
0.7:2.3:4	(Pb, Bi)Te+(Pb, Bi)$_3$Te$_4$ +(Pb, Bi)$_5$Te$_7$+(Pb, Bi)$_7$Te$_{10}$	(Pb, Bi)Te+(Pb, Bi)$_3$Te$_4$
0.9:2.1:4	(Pb, Bi)Te +(Pb, Bi)$_3$Te$_4$ +(Pb, Bi)$_5$Te$_7$+(Pb, Bi)$_7$Te$_{10}$	**(Pb, Bi)$_3$Te$_4$**
1.1:1.9:4	(Pb, Bi)Te+(Pb, Bi)$_3$Te$_4$ + (Pb, Bi)$_5$Te$_7$+(Pb, Bi)$_7$Te$_{10}$	(Pb, Bi)Te+(Pb, Bi)$_3$Te$_4$
1.3:1.7:4	(Pb, Bi)Te+(Pb, Bi)$_3$Te$_4$+ (Pb, Bi)$_5$Te$_7$+(Pb, Bi)$_7$Te$_{10}$	(Pb, Bi)Te+(Pb, Bi)$_3$Te$_4$
0.85:4.15:7	(Pb, Bi)$_3$Te$_4$+(Pb, Bi)$_5$Te$_7$ +(Pb, Bi)$_7$Te$_{10}$	(Pb, Bi)$_3$Te$_4$(traces) + (Pb, Bi)$_5$Te$_7$+(Pb, Bi)$_7$Te$_{10}$ (unobservable)
1:4:7	(Pb, Bi)$_3$Te$_4$+(Pb, Bi)$_5$Te$_7$ +(Pb, Bi)$_7$Te$_{10}$	(Pb, Bi)$_3$Te$_4$+(Pb, Bi)$_5$Te$_7$
1.15:3.85:7	(Pb, Bi)$_3$Te$_4$+(Pb, Bi)$_5$Te$_7$ +(Pb, Bi)$_7$Te$_{10}$	(Pb, Bi)$_3$Te$_4$+(Pb, Bi)$_5$Te$_7$
1.35:3.65:7	(Pb, Bi)$_3$Te$_4$+(Pb, Bi)$_5$Te$_7$	**(Pb, Bi)$_3$Te$_4$**

Two different formulas were attempted, (Pb, Bi)$_3$Te$_4$ and (Pb, Bi)$_5$Te$_7$. In the (Pb, Bi)$_3$Te$_4$ system, the atomic percentage of Te is 57% constantly. When Pb/Bi ratio is around 0.30, the final products are (Pb, Bi)$_3$Te$_4$ and (Pb, Bi)$_5$Te$_7$. When Pb/Bi ratio is around 0.43, (Pb, Bi)$_3$Te$_4$ is the only product. Both (Pb, Bi)$_3$Te$_4$ and (Pb, Bi)Te are present when Pb/Bi ratio is around 0.58. In the (Pb, Bi)$_3$Te$_4$ system, (Pb, Bi)$_7$Te$_{10}$ showed up in the intermediate products, but during annealing, it reacted with (Pb, Bi)Te to form either (Pb, Bi)$_3$Te$_4$ or (Pb, Bi)$_5$Te$_7$. In the (Pb, Bi)$_5$Te$_7$ system, Te atom% is fixed at 58%. The experimental results indicate that in order to obtain pure (Pb, Bi)$_5$Te$_7$, Pb/Bi ratio has to be below 0.25, but the lower limit is still under investigation. In the range of Pb/Bi = 0.20 - 0.30, both (Pb, Bi)$_3$Te$_4$ and (Pb, Bi)$_5$Te$_7$ are the final products, and when Pb/Bi is around 0.37, pure (Pb, Bi)$_3$Te$_4$ can be obtained. It is interesting that when the expected product was (Pb, Bi)$_5$Te$_7$, the final product turned to adopt the structure of (Pb, Bi)$_3$Te$_4$. In order to write a balanced equation for this reaction, the composition is expressed as $Pb_{0.8}Bi_{2.2}Te_4$.

Shelimova et al. concluded that $nPbTe \cdot mBi_2Te_3$ layered compounds with n/m > 1 does not exist in bulk form[71]. The experimental results shown in Table 3.7 agree with such conclusion. Phase pure samples were very difficult to obtain in Pb-rich samples, and one of the final products in these samples was PbTe type compound. Comparing PbTe type compounds

(Figure 3.5 (a)), Bi_2Te_3 type compounds (Figure 3.5 (b)) have similar structure and coordination environment to that of the tetradymite-like layered ternaries. Therefore, other than (Pb, Bi)$_3$Te$_4$ and (Pb, Bi)$_5$Te$_7$, (Pb, Bi)$_7$Te$_{10}$ was also found (Figure 3.6 and 3.9). Although no phase pure samples for either of (Pb, Bi)$_5$Te$_7$ or (Pb, Bi)$_7$Te$_{10}$ was obtained, it is believed that it is possible to obtain phase pure samples for both compounds, but it takes much longer time than to obtain (Pb, Bi)$_3$Te$_4$. Such reactions were not attempted to confirm the assumption. In the attempted $PbBi_4Te_7$ reaction, (Pb, Bi)$_5$Te$_7$ was identified as the major phase with < 5% (Pb, Bi)$_3$Te$_4$ as the second phase. Even though from the X-ray diffraction pattern of (Pb, Bi)$_5$Te$_7$, the phase (Pb, Bi)$_7$Te$_{10}$ cannot be identified due to its tiny amount, it can be confirmed to be the third phase because (1) it was needed to balance the attempted stoichiometry, $PbBi_4Te_7$; and (2) it was found in the intermediate products (Figure 3.6 and 3.9); and (3) it was the one of the final products in the sample $Pb_{0.85}Bi_{4.15}Te_7$ (Figure 3.10). Two pure samples were obtained (Figure 7-8, and 10-11), which are also summarized in Table 3.7. The (Pb, Bi)$_3$Te$_4$ type compound was obtained in the attempted (Pb, Bi)$_5$Te$_7$ reaction, so the formula of $Pb_{1.35}Bi_{3.65}Te_7$ can be re-written as $Pb_{0.8}Bi_{2.2}Te_4$.

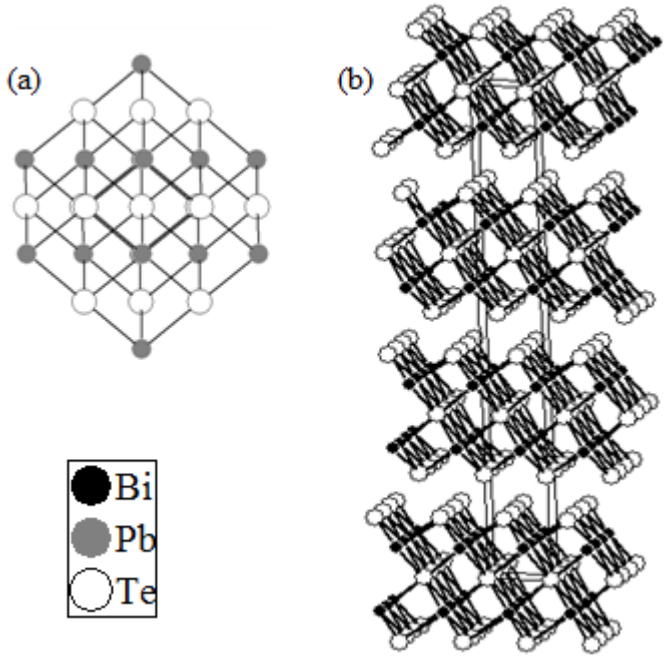

Figure 3.5 Crystal structures of (a) PbTe and (b) Bi_2Te_3.

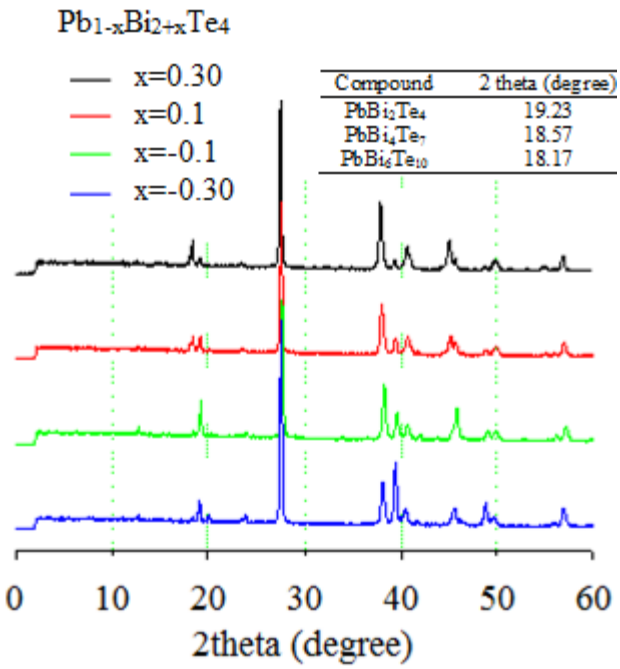

Figure 3.6 Powder X-ray diffraction pattern of intermediate products of $Pb_{1-x}Bi_{2+x}Te_4$ with x = 0.30, 0.10, –0.10 and –0.30.

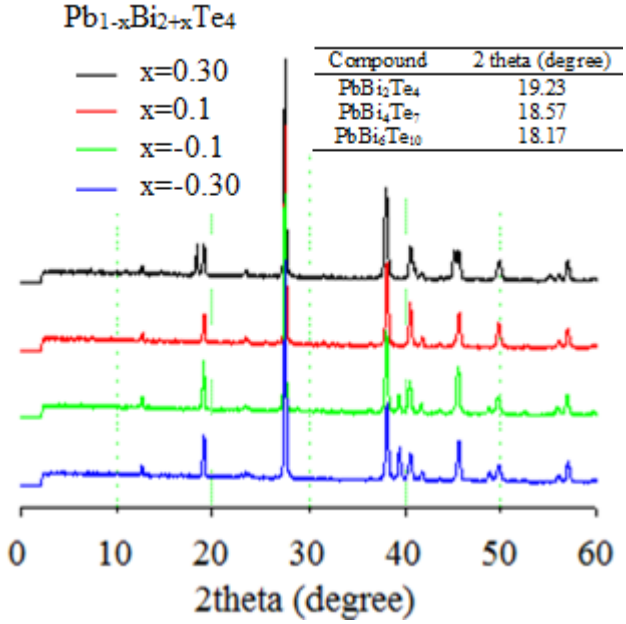

Figure 3.7 Powder X-ray diffraction pattern of equilibrium products of $Pb_{1-x}Bi_{2+x}Te_4$ with x = 0.30, 0.10, –0.10 and –0.30.

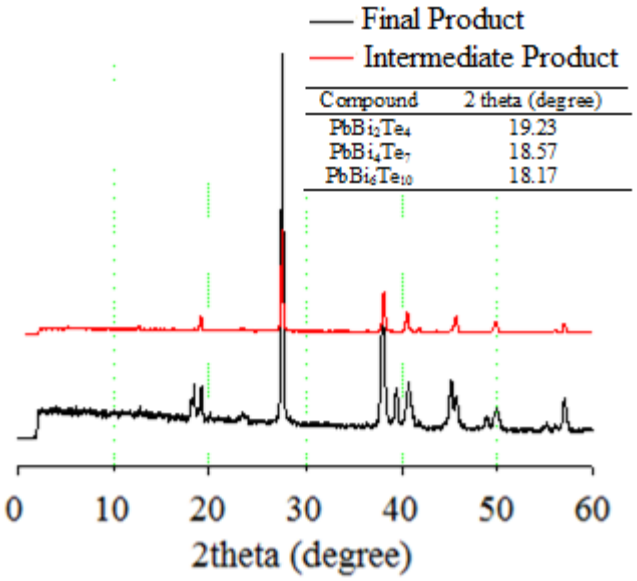

Figure 3.8 The comparison of the intermediate and equilibrium products of $Pb_{0.9}Bi_{2.1}Te_4$.

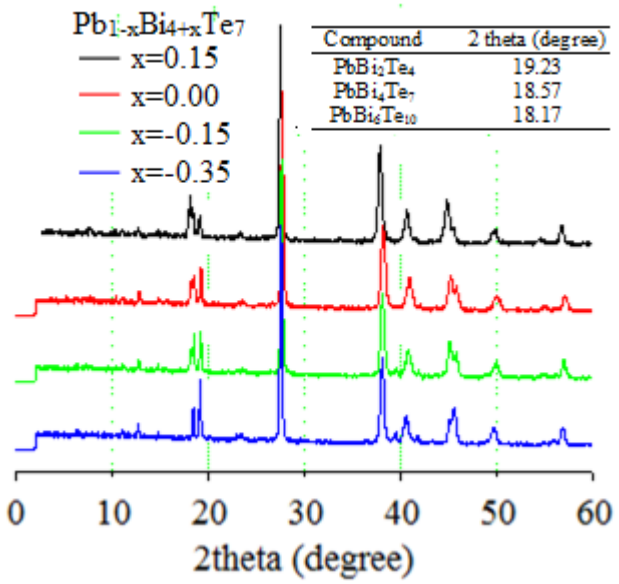

Figure 3.9 Powder X-ray diffraction pattern of intermediate products of $Pb_{1-x}Bi_{4+x}Te_7$ with x = 0.15, 0.00, –0.15 and –0.35.

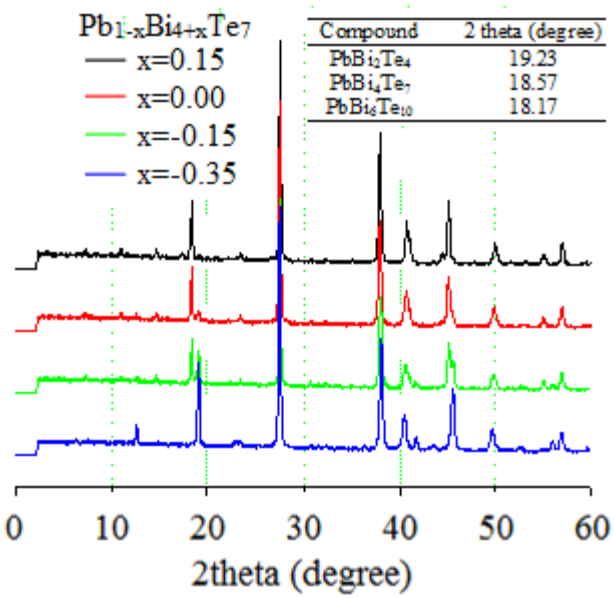

Figure 3.10 Powder X-ray diffraction pattern of equilibrium products of $Pb_{1-x}Bi_{4+x}Te_7$ with x = 0.15, 0.00, –0.15 and –0.35.

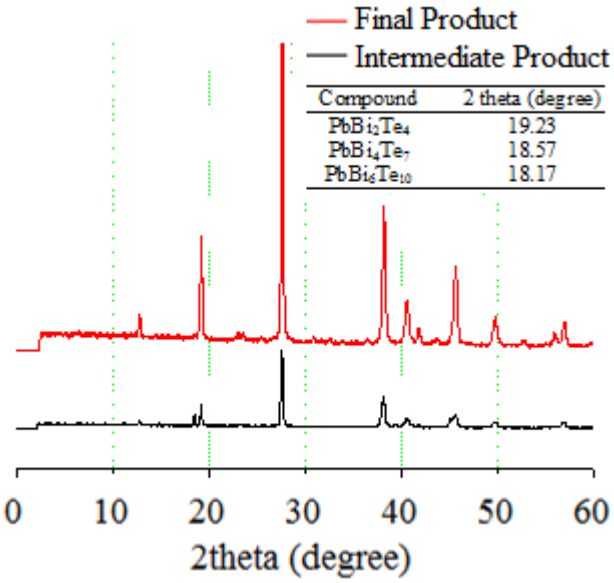

Figure 3.11 The comparison of the intermediate and equilibrium products of $Pb_{0.8}Bi_{2.2}Te_4$.

Table 3.7 Phase range summary from targeted reactions.

Pb:Bi:Te	Pb/Bi	Final Products
0.70:2.30:4.00	0.30	$(Pb, Bi)_3Te_4$+$(Pb, Bi)_5Te_7$
0.90:2.10:4.00	0.43	**$Pb_{0.9}Bi_{2.1}Te_4$**
1.10:1.90:4.00	0.58	(Pb, Bi)Te+$(Pb, Bi)_3Te_4$
1.30:1.70:4.00	0.76	(Pb, Bi)Te+$(Pb, Bi)_3Te_4$
0.85:4.15:7.00	0.20	$(Pb, Bi)_3Te_4$+$(Pb, Bi)_5Te_7$
1.00:4.00:7.00	0.25	$(Pb, Bi)_3Te_4$(traces)+$(Pb, Bi)_5Te_7$ +$(Pb, Bi)_7Te_{10}$(unobservable)
1.15:3.85:7.00	0.30	$(Pb, Bi)_3Te_4$+$(Pb, Bi)_5Te_7$
1.35:3.65:7.00	0.37	**$Pb_{0.8}Bi_{2.2}Te_4$.**

3.3 Physical Properties

3.3.1 Electrical Conductivity

All measurements were carried out on sintered cold-pressed pellets. The density of cold pressed pellet of $Pb_{0.8}Bi_{2.2}Te_4$ and $Pb_{0.9}Bi_{2.1}Te_4$ are about 80% of the estimated density. Electrical conductivity measurements on hot-pressed sample usually have much larger values in comparison with measurements on cold-pressed sample. A hot-pressed sample requires at least 4 grams powder sample. Within same period of annealing time, all attempts to obtain larger samples were failed, because it takes longer time for the system to reach equilibrium. The electrical conductivity was measured over a broad temperature range by ULVAC ZEM-3. Both samples are n-type, same as the published $PbBi_2Te_4$ and $PbBi_4Te_7$ compounds. The conductivity of each sample decreases with increasing temperature, as expected for the heavily doped semiconductors. Carrier concentration and Hall mobility were not measured. The compound $Pb_{0.8}Bi_{2.2}Te_4$ is expected to have higher carrier concentration than $Pb_{0.9}Bi_{2.1}Te_4$, because each Bi provides one more electron than Pb. But this was not confirmed experimentally, with room temperature conductivity values of 650 $\Omega^{-1}\cdot cm^{-1}$ vs. 950 $\Omega^{-1}\cdot cm^{-1}$ (Figure 3.12). $PbBi_2Te_4$ and $PbBi_4Te_7$ were reported to have high concentration of intrinsic point defects associated with deviations from stoichiometry. Anion vacancies $V_{Te}^{\bullet\bullet}$ and donors antisite defects $Bi_{Pb}^{\bullet}$ both act as electron donors[71]. Such defects influence the actual carrier concentration. The compound $Pb_{0.8}Bi_{2.2}Te_4$ was targeted to be $Pb_{1.35}Bi_{3.65}Te_7$ which has lower carrier concentration. Crystal defects also have an effect on the carrier mobility, and the more the defects, the less mobile the carriers.

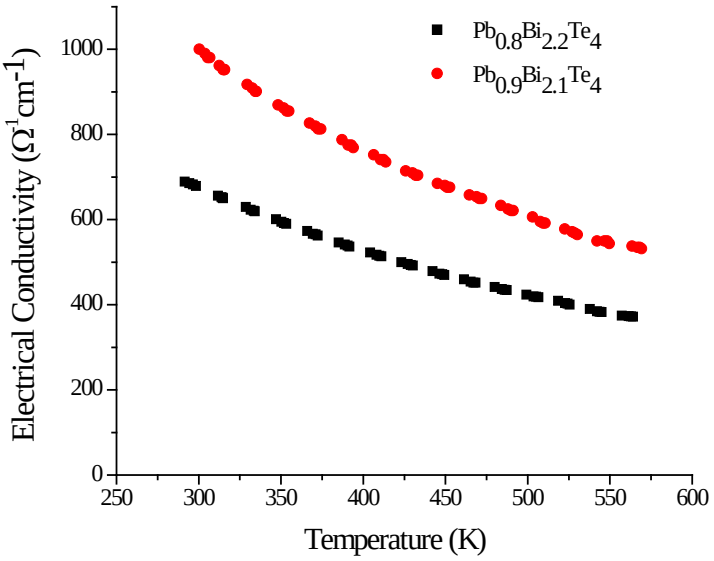

Figure 3.12 Electrical conductivity of $Pb_{0.8}Bi_{2.2}Te_4$ and $Pb_{0.9}Bi_{2.1}Te_4$.

3.3.2 Seebeck Coefficient

Figure 3.13 compares the Seebeck coefficient of $PbBi_2Te_4$ and $PbBi_4Te_7$. The compound with more Bi has the larger Seebeck coefficient value. The Seebeck coefficient is positively proportional to the effective mass of carriers, which associates with the carrier mobility. As discussed in section 3.1, the electrical conductivity measurements suggest that $Pb_{0.8}Bi_{2.2}Te_4$ has lower carrier mobility limited by the high degree of structural disordering, so it was not surprising to detect a higher Seebeck coefficient for $Pb_{0.9}Bi_{2.1}iTe_4$. The Seebeck coefficient (absolute value) increases with increasing temperature for each sample. Both $PbBi_2Te_4$ and $PbBi_4Te_7$ exhibited Seebeck coefficient maxima at different temperatures, whereas we found no local maxima between 375 and 575 K.

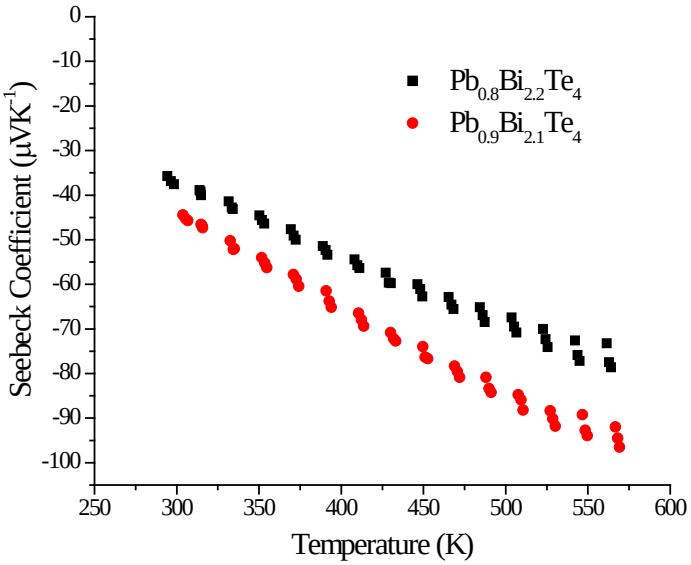

Figure 3.13 Seebeck coefficient of $Pb_{0.8}Bi_{2.2}Te_4$ and for $Pb_{0.9}Bi_{2.1}Te_4$.

3.3.3 Thermal Conductivity

The low thermal conductivity presented in Figure 3.14 may be associated with a highly complex structure and also with the presence of heavy elements (Pb and Bi). Figure 3.14 shows the total thermal conductivity and lattice contribution for $Pb_{0.8}Bi_{2.2}Te_4$ and $Pb_{0.9}Bi_{2.1}Te_4$ between 373 K and 573 K. Within this range, the thermal conductivity of both compounds is independent of the temperature. At 375 K, the thermal conductivity values of $Pb_{0.8}Bi_{2.2}Te_4$ and $Pb_{0.9}Bi_{2.1}Te_4$ are 1.15 and 1.02 $W \cdot m^{-1} \cdot K^{-1}$ respectively, comparable to the reported values of $PbBi_2Te_4$ and $PbBi_4Te_7$, 1.21 and 1.39 $W \cdot m^{-1} \cdot K^{-1}$, at room temperature[65]. The electronic contribution to the thermal conductivity estimated from the Wiedemann-Franz law is around 0.8 and 0.7 $W \cdot m^{-1} \cdot K^{-1}$ respectively, which means that the phonon contribution for both compounds is very small.

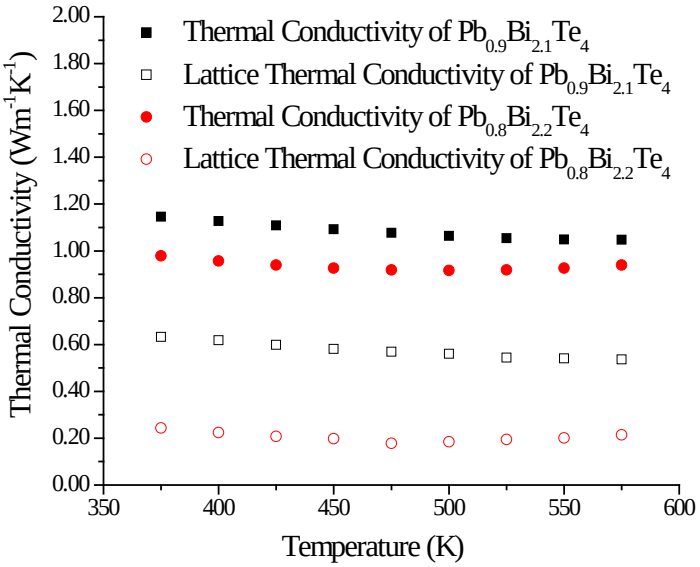

Figure 3.14 The total thermal conductivity and its corresponding lattice thermal conductivity for $Pb_{0.8}Bi_{2.2}Te_4$ and $Pb_{0.9}Bi_{2.1}Te_4$.

The dimensionless figure-of-merit, ZT, is calculated based on experimental data within the range of 375 K to 575 K (Figure 3.15). The maximum values are 0.12 and 0.32 for cold pressed $Pb_{0.8}Bi_{2.2}Te_4$ and $Pb_{0.9}Bi_{2.1}Te_4$ at 575 K, respectively. The compound $PbBi_2Te_4$ was reported to have estimated ZT value of 0.5 at 600 K[71]. Experimental data from my research show higher power factor and lower and temperature-independent thermal conductivity than the published data. It can be confirmed that with more future work, $Pb_{1+x}Bi_{2-x}Te_4$ ($0.1 < x < 0.2$) has a potential for thermoelectric application in the temperature range from 400 to 650K.

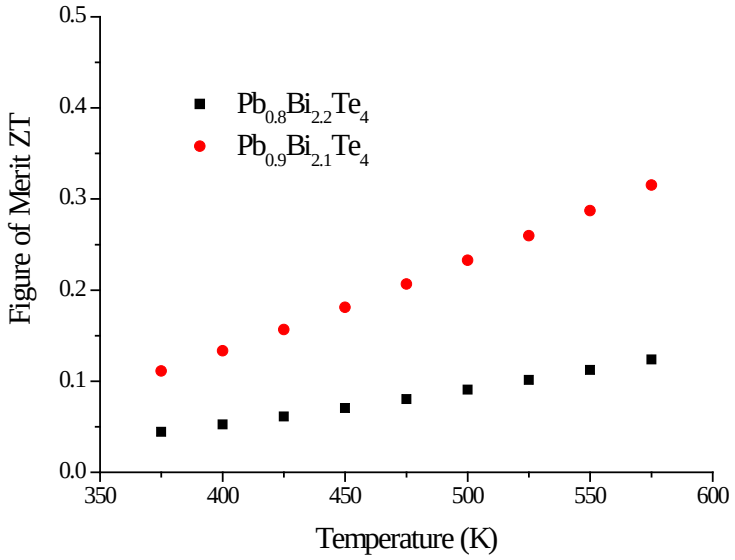

Figure 3.15 Figure-of-Merit, ZT, vs. temperature.

4. The Quaternary Derivatives of Tl_9BiTe_6

4.1 Introduction

Thallium has a high atomic mass, and its inert electron pair enhances the tendency towards distorted coordination environments[73]. These properties often lead to extremely low thermal conductivity for Tl-containing compounds[74,75]. Previous studies of these thallium compounds proved that they are advanced thermoelectric materials, especially the ternary telluride Tl_9BiTe_6[76-78]. The ternary Tl_9BiTe_6 presents high thermoelectric figure of merit[76,79]. It is interesting to notice that its outstanding thermoelectric properties fall into the range achieved within the exhaust system of automotives ($T_{max} < 500^oC$). The unit cell of Tl_9BiTe_6 is shown in Table 4.1 and Figure 4.1. The ternary compound is derived the Tl_5Te_3 family. The tetragonal unit cell of Tl_5Te_3, where Tl^+ atoms (white) occupy the site 16l, "Tl^{2+}" (half Tl^+ and half Tl^{3+}) atoms occupy site the 4c (center, checkered), and Te^{2-} atoms in black take the 8h and 4a positions. In the ternary compound, Tl_9BiTe_6, Tl^{3+} atoms on the 4c site are substituted by Bi^{3+}. Both Tl^+ and Bi^{3+} on site 4c have an occupancy of 50% (see Table 4.2). In contract to Tl_9BiTe_6, the 4c sites in $Tl_8Pb_2Te_6$ are solely occupied by the Pb^{2+} cation[79].

Table 4.1 Structural information on Tl_9BiTe_6[80] and $Tl_8Pb_2Te_6$[79] from previous studies.

Compound	Space Group	Lattice Dimension
Tl_9BiTe_6[80]	*I*4/*mcm*	*a* = 8.855(2)Å *c* =13.048(4) Å
$Tl_8Pb_2Te_6$[81]	*I*4/*mcm*	*a* = 8.841(2)Å *c* =13.056(3) Å

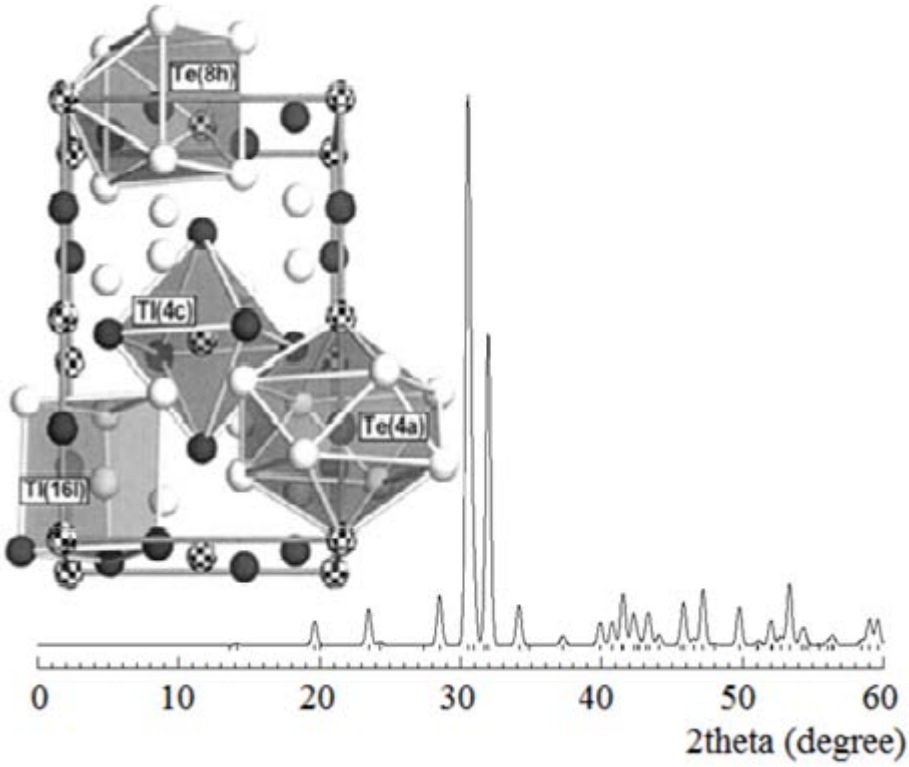

Figure 4.1 Calculated powder X-ray diffraction pattern of Tl_9Te_6 and the unit cell of Tl_5Te_3[80].

Table 4.2 Detailed structural information on Tl_9BiTe_6 from a previous study[80].

Atom	Atom Site (x, y, z)	Wyckoff Position	Occupancy
Bi^{3+}	0 0 0	4c	0.5
Tl^{+}	0 0 0	4c	0.5
Tl^{+}	0.1466(2) 0.6466(2) 0.1592(1)	16l	1
Te^{2+}	0. 0. 0.250	4a	1
Te^{2+}	0.3375(3) 0.8375(3) 0	8h	1

The present thermoelectric properties (synthesized and zone refined compounds) are summarized in Tables 4.3 and 4.4. The positive Seebeck coefficient indicates that in both Tl_9BiTe_6 and $Tl_8Pb_2Te_6$, holes are the major carriers. The power factor $S^2\sigma$ of Tl_9BiTe_6 increases until 200 K, then remains constant until 500 K with its value around 1 $mW/m\cdot K^2$. This can be explained by its constant Hall mobility and decreasing carrier mobility with temperature[76,79]. Although the electrical property of zone refined Tl_9BiTe_6 is much better than most of Tl-containing compounds, it is still not as good as other thermoelectric materials, such as Bi_2Te_3, $S^2\sigma = 4$ $mWm\cdot K^{-2}$ [79] . Therefore, a systematic doping work on the p-type compound needs to be carried out to further improve the electrical properties.

Table 4.3 Published properties of hot-pressed Tl_9BiTe_6[76].

T (K)	S ($\mu V \cdot K^{-1}$)	σ ($\Omega^{-1} \cdot cm^{-1}$)	κ ($W \cdot m^{-1} \cdot K^{-1}$)	Estimated ZT
300	160	167	0.39	0.33
400	200	143	0.39	0.62
500	220	125	0.39	0.78
590	235	100	0.39	0.80

Table 4.4 Published properties of zone refined Tl_9BiTe_6[79].

T (K)	S ($\mu V \cdot K^{-1}$)	σ ($\Omega^{-1} \cdot cm^{-1}$)	κ ($W \cdot m^{-1} \cdot K^{-1}$)	Estimated ZT
200	180	263	0.60	0.28
300	275	133	0.50	0.60
400	325	100	0.45	0.93
500	399	60	0.40	1.3

The thermal conductivity has two contributions, the electronic contribution and lattice contribution. The electronic contribution is positively related to the electrical conductivity, so it is not wise to lower the electronic thermal conductivity. Instead, by reducing the lattice thermal conductivity, the total thermal conductivity will be smaller while the electrical conductivity ideally remains unaffected. The lattice thermal conductivity is controlled by the bond strength and crystal structure of a material. In the Tl_9BiTe_6 compound, the distribution of Tl^+ and Bi^{3+} is rather random. In comparison with the ordered compound $Tl_8Pb_2Te_6$ (0.72 W/m·K at 300 K), Tl_9BiTe_6 exhibits much lower thermal conductivity (0.39W/m·K at 300K). The different atomic masses of Pb and Bi (~2%) can be excluded as an important scattering mechanism to cause such difference[79]. Instead, the difference in the valence states on the 4c site, Bi^{3+} and Tl^+ which causes the disorder on the 4c site has a significant influence on the thermal conductivity[79,82-84].

Another concept ‘Nanocomposites in bulk materials’ was proposed. This can be viewed as phase pure on a large scale; it, however, is ‘inhomogeneous’ at the nanoscale[34,35]. It is believed that phonon thermal conductivity is lower in such a material. So one of the best ways to improve the TE properties is to lower the lattice thermal conductivity by introducing nanodomains (See 1.3.3. Bulk materials with nano-composites). The postulated quaternary thermoelectric materials constitute a new research area, and based on previous studies on Tl_9BiTe_6, and $Tl_8Pb_2Te_6$, the nanocomposites are highly expected in quaternary compounds

$Tl_8(Tl^+, Pb^{2+}, Bi^{3+})_2Te_6$.

The dimensionless figure of merit ZT for Tl_9BiTe_6 shows a maximum at 590 K, followed by a decrease due to its decreasing electrical conductivity and increasing thermal conductivity after 600 K. The ZT value for zone refined Tl_9BiTe_6 reaches 1.2 at 500 K. It can be confirmed that in the range of 400 - 600 K, quaternary $Tl_8(Tl, Pb, Bi)_2Te_6$ are good candidates for thermoelectric application. In the quaternary $Tl_8(Tl, Pb, Bi)_2Te_6$ system, possible doping works can be carried out and more complex structures are expected to further improve the thermoelectric performance.

Modifying Tl_9BiTe_6 by addition of lead to substitute the Tl^+ and Bi^{3+} on 4c site and finally obtaining quaternary compounds with competitive electrical properties and even more complex crystal structure is the motivation of this research. Several reactions with different atomic ratios as listed in Table 4.5 were carried out. All x of the compounds were controlled so that the compounds have charge carrier concentration in the range of 10^{20} - 10^{21} cm^{-3}. The first three reactions all came out with side products, indicating that the structure cannot hold that many electrons. The $Tl_8Tl_{0.66}Pb_{1.33-x}Bi_xTe_6$ system has apparently better thermoelectric performance in comparison with $Tl_8Tl_{0.33}Pb_xBi_{1.80-x}Te_6$, therefore the former system was focused on. Its synthesis, structural analysis, thermoelectric properties are discussed in the following sections.

Table 4.5 Targeted quaternary compounds.

Nominal Composition	x Value	Final Products
$Tl_8Pb_xBi_{2-x}Te_6$	0.10 - 0.20	$Tl_8(Tl, Pb, Bi)_2Te_6$+$(Tl, Pb, Bi)_2Te_2$
$Tl_8Tl_{0.1}Pb_xBi_{1.90-x}Te_6$	0.10 - 0.20	$Tl_8(Tl, Pb, Bi)_2Te_6$+$(Tl, Pb, Bi)_2Te_2$
$Tl_8Tl_{0.2}Pb_xBi_{1.80-x}Te_6$	0.10	$Tl_8(Tl, Pb, Bi)_2Te_6$+$(Tl, Pb, Bi)_2Te_2$
$Tl_8Tl_{0.33}Pb_xBi_{1.80-x}Te_6$	1.00 - 1.36	Target obtained
$Tl_8Tl_{0.67}Pb_xBi_{1.33-x}Te_6$	0.45 - 1.00	Target obtained when x>0.50

4.2 Synthesis and Structural Analysis

4.2.1 Synthesis and Analysis

The $Tl_{8.67}Pb_xBi_{1.33-x}Te_6$ compounds were obtained by direct synthesis of stoichiometric amounts of powders of high purity elements (Tl, granules, 6mm, 99.999%, Alfa Aesar, Pb, granules, 3mm, 99.9%, Alfa Aeasar, Bi, powder, -100 mesh, 99.5%, Alfa Aesar; Te, granules, -3mm to +50 mesh, 99.99%, Alfa Aesar) in evacuated quartz tubes. The starting materials were heated at 923 K for 6 hours and then slowly cooled down. The obtained ingots were crushed and pressed into pellets, followed by annealing at 673 K for a few days to improve the purity. The final products were then crushed into fine powders for the structural analysis by the powder X-ray diffraction method carried out at room temperature using INELs powder diffractometer with position-sensitive-detector.

The chemical compositions of the samples were determined by energy dispersive X-ray analysis. Le Bail refinements were carried out to obtain the lattice parameters of the series. When x is smaller than 0.45 (Figure 4.2), the layered compound $(Tl, Pb, Bi)_2Te_2$ (i.e. substitution variants of $TlBiTe_2$, -$NaFeO_2$ type) consistently shows up as a side product in the final product, and the compounds with x greater than 1 do not have competitive electrical properties in the preliminary study. Therefore, samples with x = 0.50, 0.6, 0.66, 0.80 and 1.00 were chosen for further study (Table 4.6). The pure samples were hot pressed sample, using spark plasma sintering technique by Dr. Nygren, in Univeristy of Stockholm, Sweden. All electrical conductivity and Seebeck Coefficient measurements were carried out on the hot pressed pellets, which have densities of 90% of the theoretical values[53]. The thermal conductivity measurements were performed on the sintered cold pressed pellets, with densities around 80% of the theoretical values.

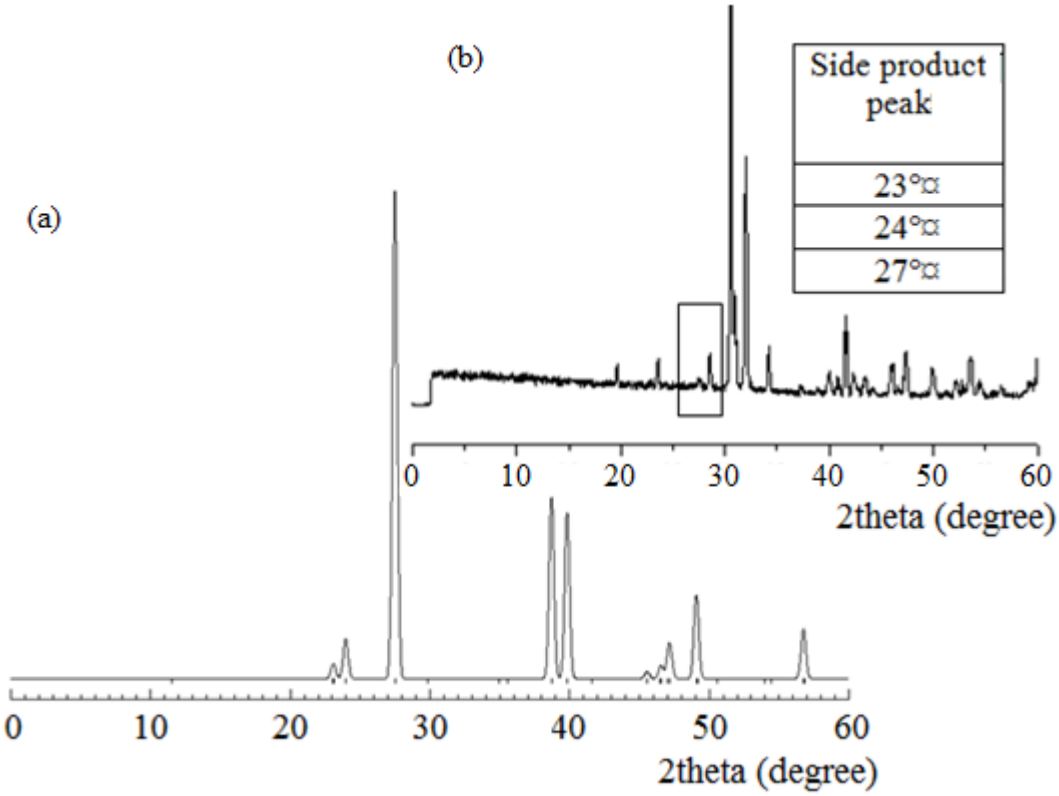

Figure 4.2 Powder X-ray diffraction patterns of (a) calculated $TlBiTe_2$; (b) synthesized $Tl_{8.67}Pb_{0.44}Bi_{0.89}Te_6$ containing side product.

A sample of nominal composition of $Tl_{8.33}Pb_{1.115}Bi_{0.555}Te_{6.00}$ was sent to McMaster University, Ontario, Canada for High Resolution Transmission Electron Microscope (HRTEM) analysis. Because the neighboring elements Tl, Pb and Bi cannot be differentiated from one to another, the sample looks very homogeneous and highly crystalline.

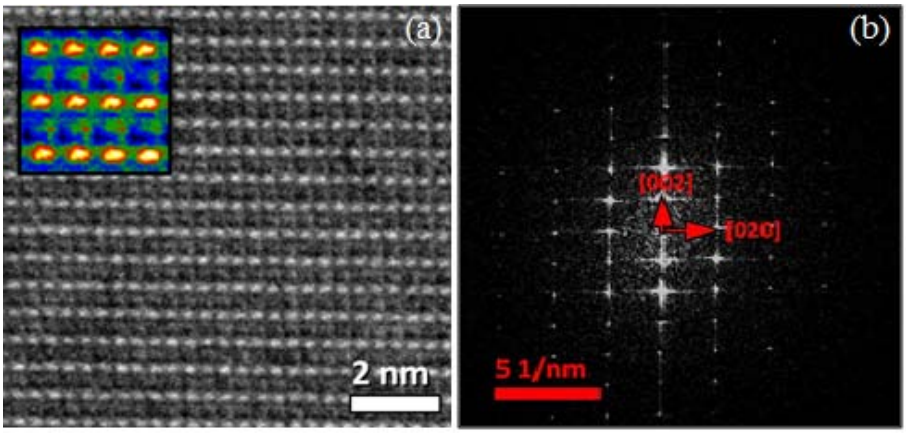

Figure 4.3 (a) A HRTEM image of the crystal lattice viewed down the [101] zone axis; (b) the Fourier transform of the lattice image with labeled lattice reflections.

Table 4.6 Targeted $Tl_{8.67}Pb_xBi_{1.33-x}Te_6$ and corresponding products.

Nominal Composition ($Tl_{8.67}Pb_xBi_{1.33-x}Te_6$)	Final Products
x = 0.50	$Tl_{8.67}Pb_{0.50}Bi_{0.83}Te_6$
x = 0.60	$Tl_{8.67}Pb_{0.60}Bi_{0.67}Te_6$
x = 0.66	$Tl_{8.67}Pb_{0.66}Bi_{0.67}Te_6$
x = 0.80	$Tl_{8.67}Pb_{0.80}Bi_{0.53}Te_6$
x = 1.00	$Tl_{8.67}Pb_{1.00}Bi_{0.33}Te_6$

4.2.2 Le Bail Refinement

Each powder sample of $Tl_{8.67}Pb_xBi_{1.33-x}Te_6$ series was scanned for 2 hours at room temperature, and X-ray diffraction data were collected for further structural analysis. Silicon power was added into each sample as internal reference. Refinements were performed on the samples as listed in Table 4.7 to obtain lattices parameters. The Le Bail method was applied for the refinements by using the program GSAS. The cell and profile parameters were the only parameters refined in Le Bail method. Since from the X-ray diffraction data, the difference between Tl, Pb, and Bi cannot be distinguished, it is not necessary to refine the mixed occupancy on 4c site. The refinement results in Table 4.7 and Figure 4.4 - 4.8 in comparison with published cell dimensions of $Tl_{10}Te_6$ and its derivatives show a trend that with unchanged thallium and tellurium contents, higher lead contents cause smaller unit cells. This is mainly due to the different covalent radii, which are 1.46 Å for Pb and 1.48 Å for Bi[85].

Table 4.7 Lattice parameters obtained by Le Bail refinements in comparison with published cell dimensions.

Tl:Pb:Bi:Te	Lattice Parameters (Å)	V (Å^3)	Calculated ρ (g·cm^{-3})
10:0:0:6[86]	a=b=8.917(3) c=12.613(3)	1002.9	9.3
9:0:1:6[87]	a=b=8.855(2) c=13.048(4)	1023.11	9.13
8:2:0:6[81]	a=b=8.841(2) c=13.056(3)	1020.5	9.16
8.67:0.50:0.83:6.00	a=b=8.85357(9) c=13.0514(2)	1023.04(1)	9.13
8.67:0.60:0.73:6.00	a=b=8.842(1) c=13.033(2)	1019.0(4)	9.13
8.67:0.66:0.67:6.00	a=b=8.8381(1) c=13.0057(5)	1015.89(3)	9.14
8.67:0.80:0.53:6.00	a=b=8.8261(2) c=12.9552(7)	1009.20(5)	9.27
8.67:1.0:0.33:6.00	a=b=8.8234(7) c=12.946(1)	1007.9(1)	9.31

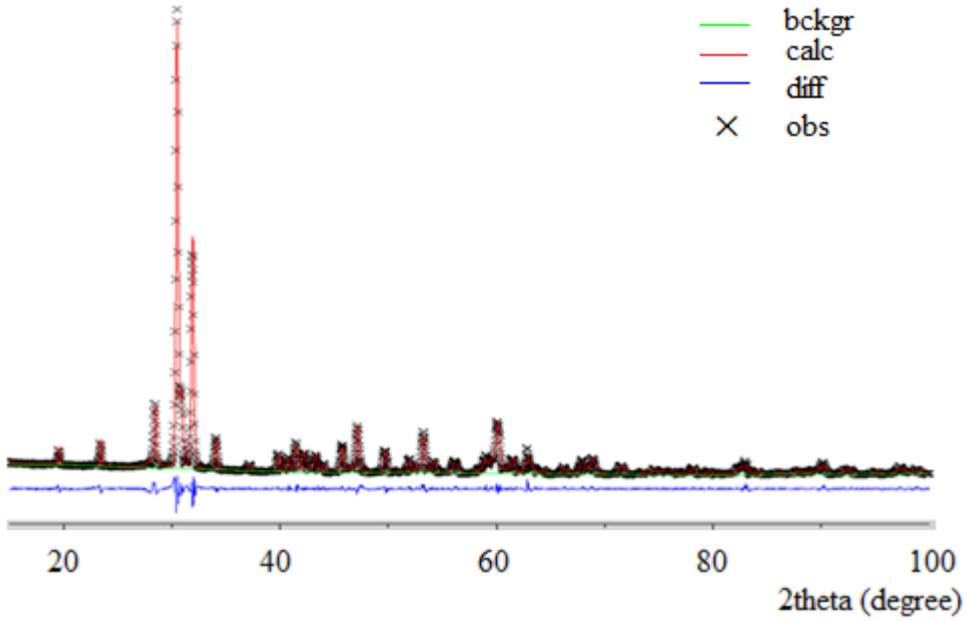

Figure 4.4 Le Bail refinement with powder X-ray diffraction data for $Tl_{8.67}Pb_{0.50}Bi_{0.83}Te_6$.

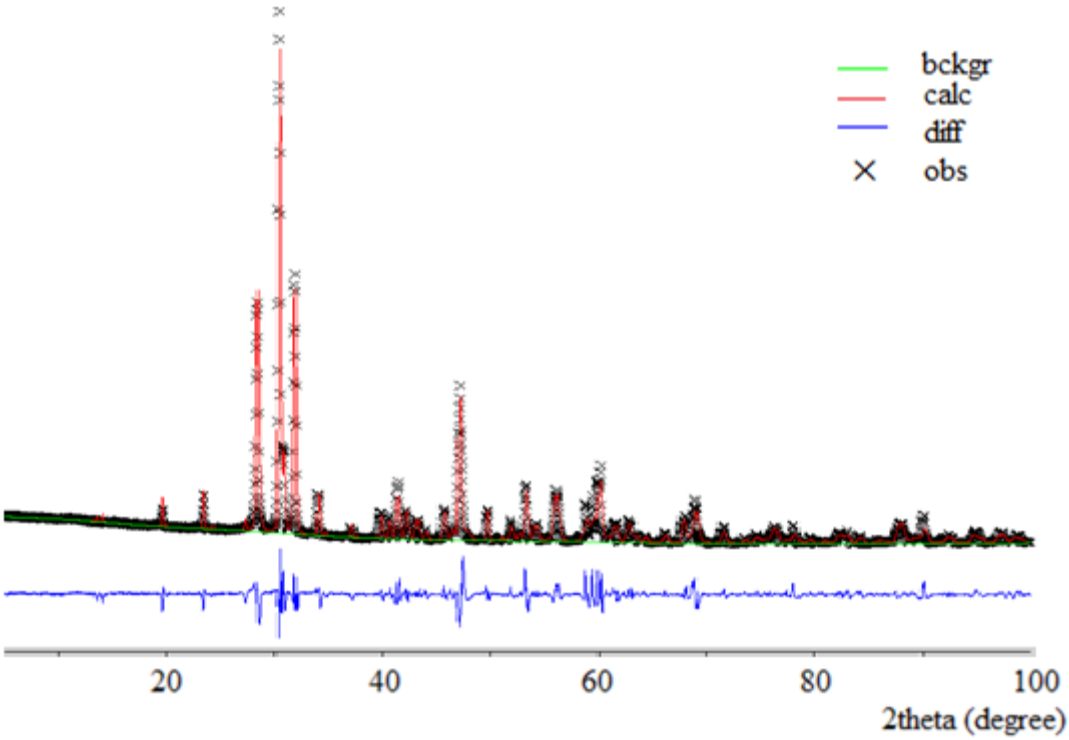

Figure 4.5 Le Bail refinement with powder X-ray diffraction data for $Tl_{8.67}Pb_{0.60}Bi_{0.67}Te_6$.

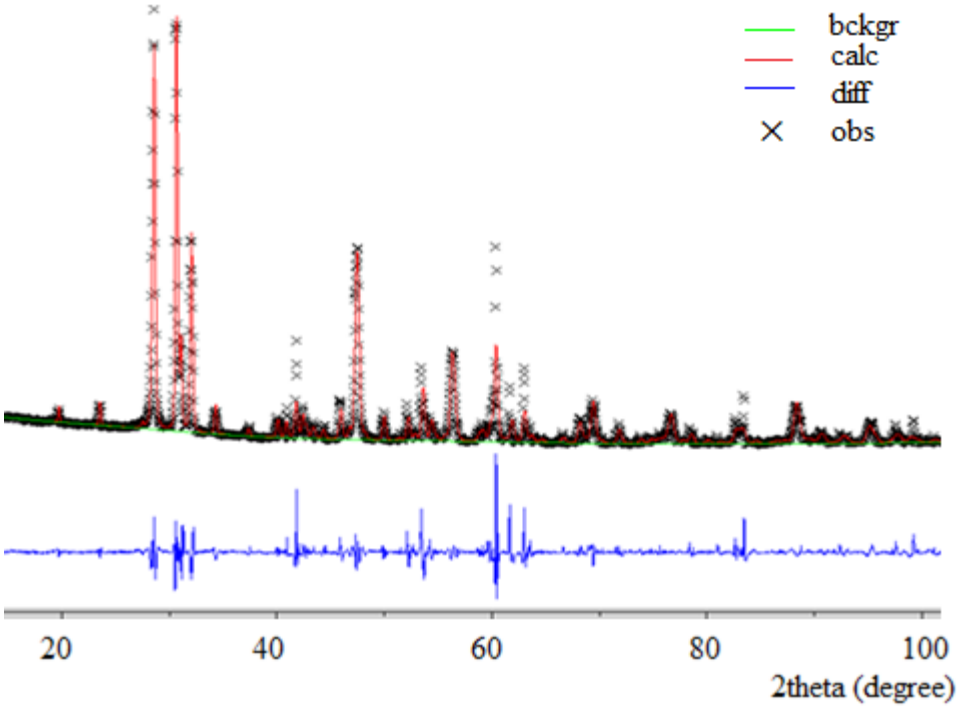

Figure 4.6 Le Bail refinement with powder X-ray diffraction data for $Tl_{8.67}Pb_{0.66}Bi_{0.67}Te_6$.

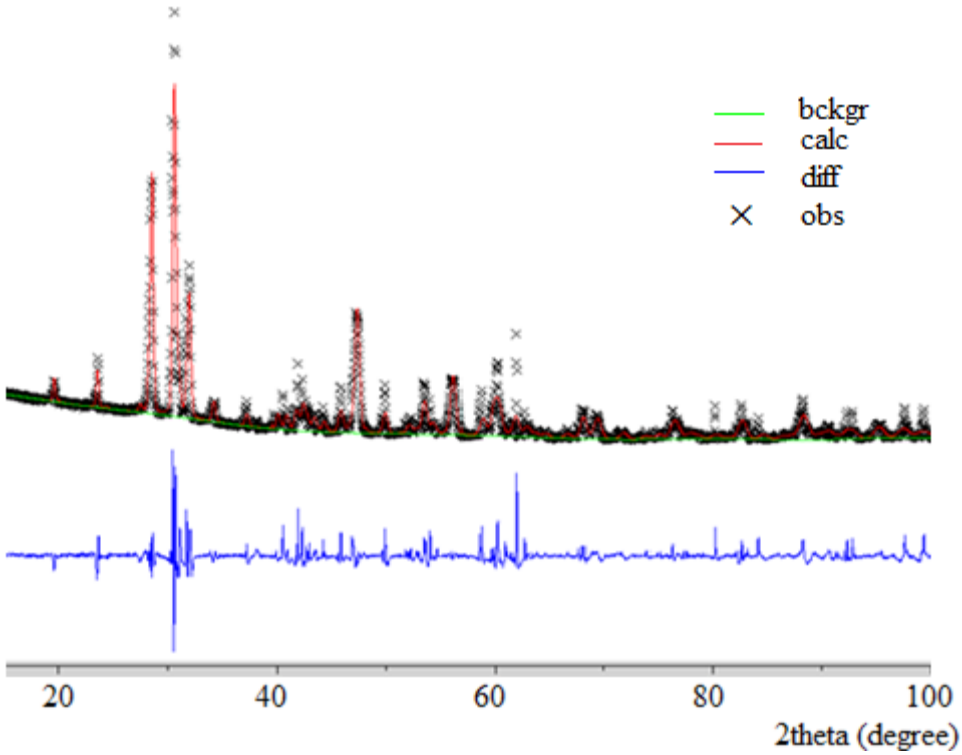

Figure 4.7 Le Bail refinement with powder X-ray diffraction data for $Tl_{8.67}Pb_{0.80}Bi_{0.53}Te_6$.

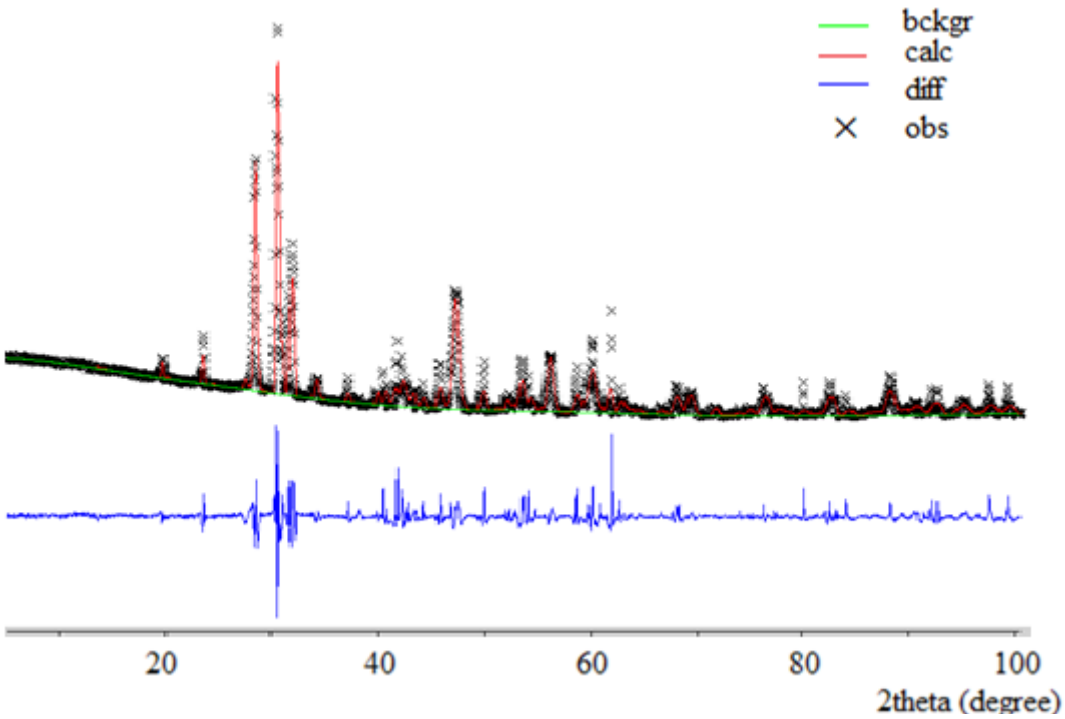

Figure 4.8 Le Bail refinement with powder X-ray diffraction data for $Tl_{8.67}Pb_{1.0}Bi_{0.33}Te_6$.

4.3 Thermoelectric Properties of the $Tl_{8.67}Pb_xBi_{1.33-x}Te_6$ Series

4.3.1 Electrical Conductivity

Generally, the electrical conductivity and thus the carrier concentration decrease with increasing bismuth content (Figure 4.9). So the lowest electrical conductivity was observed for the compound $Tl_{8.67}Pb_{0.50}Bi_{0.83}Te_6$, 50 $\Omega^{-1}\cdot cm^{-1}$ at room temperature. The electrical conductivity of $Tl_{8.67}Pb_{0.50}Bi_{0.83}Te_6$ increases very slowly with temperature, suggesting that the compound behaves like a semiconductor. All the other compounds show decreasing electrical conductivity with temperature, indicating that the mobility decrease outweighs the possible changes in charge carrier concentration with increasing temperature. The compound with the highest Pb content, x = 1.0, has the biggest electrical conductivity, 1700 $\Omega^{-1}\cdot cm^{-1}$. The electrical conductivity curves of $Tl_{8.67}Pb_{0.66}Bi_{0.67}Te_6$ and $Tl_{8.67}Pb_{0.80}Bi_{0.53}Te_6$ are roughly equivalent despite the nominal difference in Bi content and thus in the carrier concentration. One explanation may be that the electrical conductivity is not a function of only the carrier concentration but also the carrier mobility, and the carrier mobility is a complex factor that depends on electronic structure, scattering mechanism, and anisotropy. On the other hand, the uncertainties in sample composition and conductivity measurement may have contributed as well.

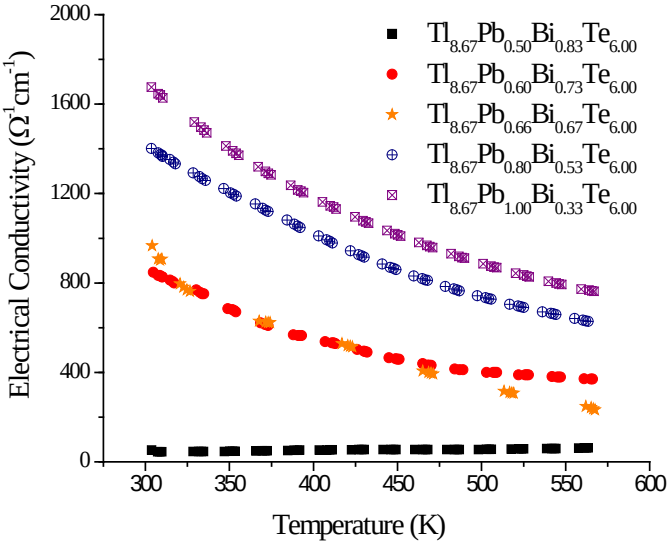

Figure 4.9 The electrical conductivity of $Tl_{8.67}Pb_xBi_{1.33-x}Te_6$ with x = 0.50, 0.60, 0.66, 0.80 and 1.0.

4.3.2 Seebeck Coefficient

Positive Seebeck coefficient values were obtained in all cases (Figure 4.10), indicating that holes are the dominant charge carriers in these materials.

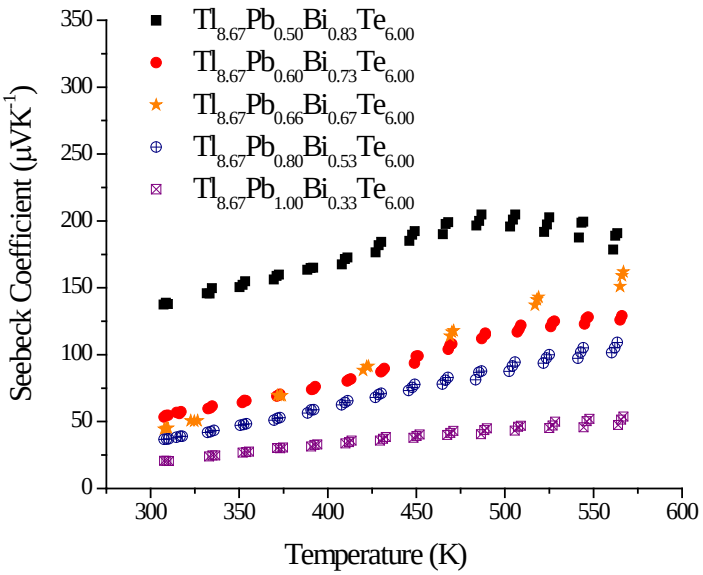

Figure 4.10 The Seebeck coefficient of $Tl_{8.67}Pb_xBi_{1.33-x}Te_6$ with x = 0.50, 0.60, 0.66, 0.80 and 1.0.

The Seebeck coefficient of $Tl_{8.67}Pb_{0.50}Bi_{0.83}Te_6$ increases with temperature and reaches its maximum value of 200 μV/K at 475 K, while the other compounds have monotonically increasing Seebeck coefficient. As more Pb is substituted by Bi, more electrons are added. In such materials, holes are the dominant charge carriers, and an increasing electron concentration will result in a decrease in the hole concentration. The highest Seebeck coefficient was found in the compound $Tl_{8.67}Pb_{0.50}Bi_{0.83}Te_6$, which has the highest bismuth content and hence the smallest amount of holes. With the Seebeck coefficient being inversely related to the carrier concentration, this was to be expected.

However, the material with x = 0.66 is formally electron precise, i.e. the band gap falls directly into the Fermi level, as the formula $(Tl^+)_{8.67}(Pb^{2+})_{0.66}(Bi^{3+})_{0.67}(Te^{2-})_6$ implies. Therefore, one might expect the samples with x < 0.66 to be n-type, which however was not experimentally observed. The same phenomenon also occurs in $Bi_{2+x}Te_{3-x}$ (Figure 4.11). It is interesting to notice that both n-type and p-type conducting properties were found in the

system, and when the compound is formally neutral, the Seebeck coefficient (of the sample with 60 at-% Te) is positive[88].

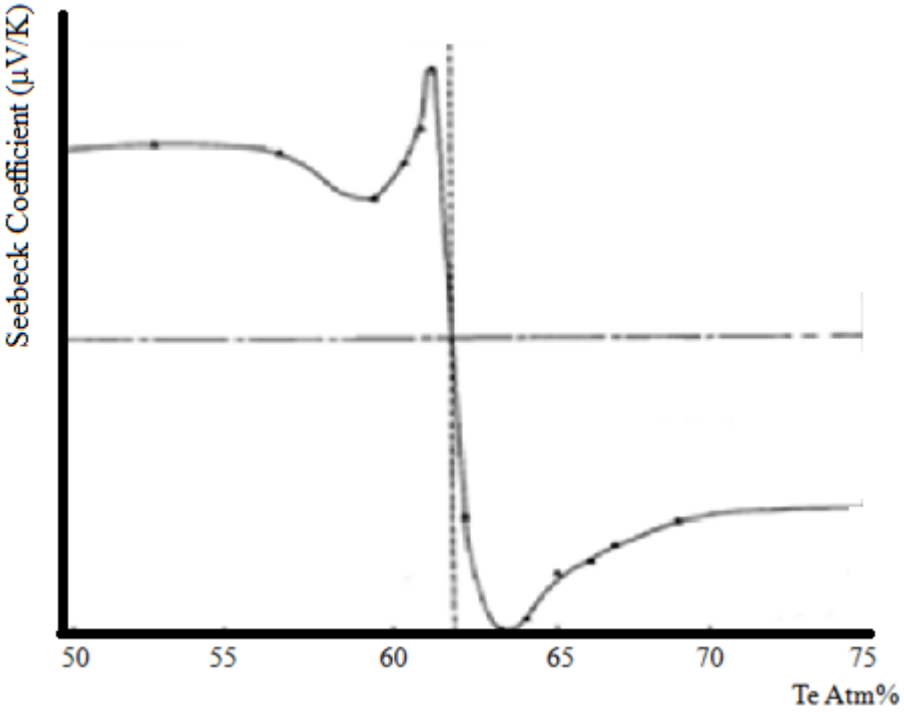

Figure 4.11 Seebeck coefficient for both n- and p-type Bi_2Te_3[88].

It was not possible to create n-type conduction in the $Tl_{8.67}Pb_xBi_{1.33-x}Te_6$ series. When x is smaller than 0.5, $TlBiTe_2$ type compounds were found as side products, indicating that 9-1-6 structure collapses when too many electrons are doped into the system. On the other hand, thermoelectric properties of the compounds without Bi are not competitive.

4.3.3 Thermal Conductivity

All $Tl_{8.67}Pb_xBi_{1.33-x}Te_6$ compounds are low (Figure 4.12) in thermal conductivity. No strong temperature dependence was found. Both contributions from the electronic and lattice thermal conductivity need to be taken into account. It was not surprising to find the highest thermal conductivity in the compound with the smallest Bi content (large electronic contribution). The lattice conductivity was calculated by using the Wiedemann-Franz Law (Table 4.8), but the uncertainty of the values is large due to the Lorenz number 2.4×10^{-8} $J^2C^{-2}K^{-2}$ used for calculation. The Lorenz number is only roughly constant and is not exactly

the same for all materials. Even for the same material at different temperatures, the Lorenz number varies. Because both $Tl_{8.67}Pb_{0.50}Bi_{0.83}Te_6$ and $Tl_{8.67}Pb_{0.60}Bi_{073}Te_6$ have very low thermal conductivity, accurate Lorenz values are needed to obtain reliable lattice thermal conductivity.

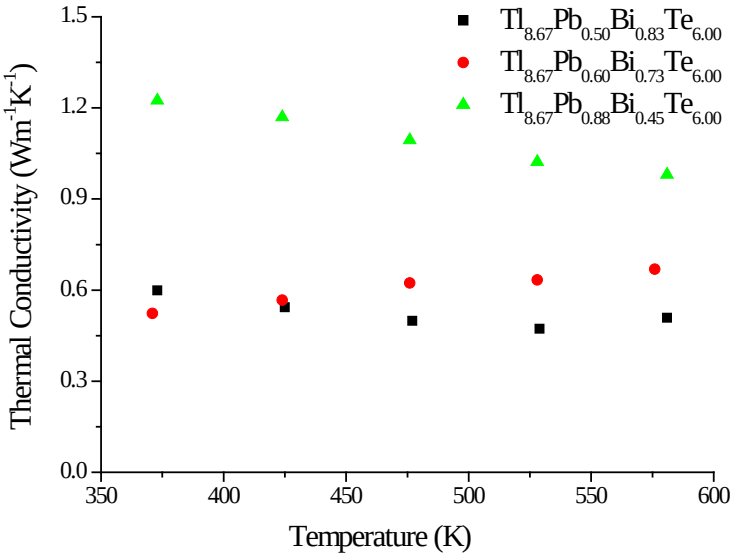

Figure 4.12 The total thermal conductivity of $Tl_{8.67}Pb_xBi_{1-x}Te_6$ with x = 0.50, 0.60 and 0.88.

Table 4.8 Lattice thermal conductivity of samples of $Tl_{8.67}Pb_{0.50}Bi_{0.83}Te_6$ and $Tl_{8.67}Pb_{0.60}Bi_{0.67}Te_6$.

T (K)	$Tl_{8.67}Pb_{0.50}Bi_{0.83}Te_6$(W·m^{-1}·K^{-1})	$Tl_{8.67}Pb_{0.60}Bi_{0.67}Te_6$ (W·m^{-1}·K^{-1})
375	0.56	0.09
400	0.51	0.15
425	0.48	0.20
450	0.45	0.26
475	0.43	0.30
500	0.42	0.33
525	0.41	0.35
550	0.41	0.36
575	0.41	0.36

4.3.4 The Dimensionless Figure of Merit and Power Factor

The figure of merit of $Tl_{8.67}Pb_xBi_{1.33-x}Te_6$ is comparable to the reported ZT (Figure 4.13 and Table 4.9 and 4.10) for $Tl_{10}Te_6$ and its derivatives. The electrical conductivity is greatly

improved while the Seebeck coefficient is also reasonably good. Unlike Tl_9BiTe_6, the power factor, $S^2\sigma$, of the quaternary compounds increases with temperature (Table 4.11), and it can almost reach $1mW\cdot m^{-1}\cdot K^{-2}$ at high temperature. By comparing the power factor of all compounds, it appears that the best electrical property can be achieved when x is between 0.6 and 1.0. The ZT values of $Tl_{8.67}Pb_{0.50}Bi_{0.83}Te_6$ and $Tl_{8.67}Pb_{0.60}Bi_{0.73}Te_6$ imply that the quaternary compounds have great potential to be good thermoelectric materials in the future.

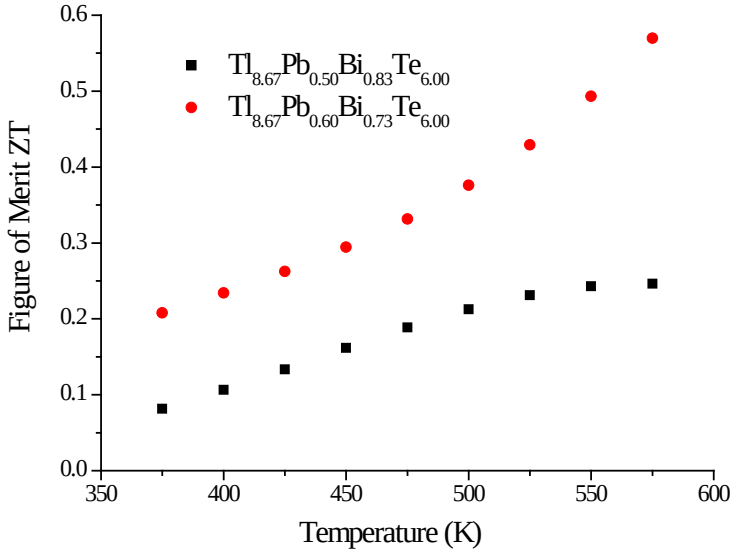

4.13 Figure-of-Merit, ZT vs. temperature for $Tl_{8.67}Pb_{0.50}Bi_{0.83}Te_6$ and $Tl_{8.67}Pb_{0.60}Bi_{0.67}Te_6$.

Table 4.9 Thermoelectric properties of $Tl_{8.67}Pb_{0.50}Bi_{0.83}Te_6$.

T (K)	$S^2\sigma$ ($mW\cdot m^{-1}\cdot K^{-2}$)♣	κ ($W\cdot m^{-1}\cdot K^{-1}$)♥	ZT
375	0.13	0.6	0.081
400	0.15	0.56	0.11
425	0.17	0.54	0.13
450	0.18	0.51	0.16
475	0.29	0.50	0.19
500	0.21	0.49	0.21
525	0.21	0.49	0.23
550	0.22	0.49	0.24
575	0.21	0.50	0.25

Table 4.10Thermoelectric properties of $Tl_{8.67}Pb_{0.60}Bi_{0.67}Te_6$.

T (K)	$S^2\sigma$ ($mW\cdot m^{-1}\cdot K^{-2}$)♣	κ ($W\cdot m^{-1}\cdot K^{-1}$)♥	ZT
375	0.28	0.68	0.21
400	0.43	0.73	0.23
425	0.48	0.78	0.26
450	0.54	0.83	0.29
475	0.62	0.88	0.33
500	0.70	0.93	0.38
525	0.80	0.98	0.43
550	0.92	0.10	0.49
575	1.1	0.11	0.57

Table 4.11 Power factors of $Tl_{8.67}Pb_{0.80}Bi_{0.53}Te_6$ and $Tl_{8.67}Pb_{1.00}Bi_{0.33}Te_6$.

T (K)	$S^2\sigma$ ($mW\cdot m^{-1}\cdot K^{-2}$)♣ $Tl_{8.67}Pb_{0.66}Bi_{0.67}Te_6$	$S^2\sigma$ ($mW\cdot m^{-1}\cdot K^{-2}$)♣ $Tl_{8.67}Pb_{0.80}Bi_{0.53}Te_6$	$S^2\sigma$ ($mW\cdot m^{-1}\cdot K^{-2}$)♣ $Tl_{8.67}Pb_{1.00}Bi_{0.33}Te_6$
375	0.33	0.32	0.11
400	0.39	0.45	0.12
425	0.45	0.43	0.13
450	0.49	0.49	0.14
475	0.52	0.53	0.15
500	0.55	0.59	0.16
525	0.58	0.63	0.17
550	0.60	0.69	0.18
575	0.67	0.74	0.19

Property measurements were measured on (♣)hot pressed pellets; (♥)sintered cold pressed pellets.

5. Conclusion

In this work, pure compounds $Pb_{1-x}Bi_{2+x}Te_4$ with x = 0.1 and 0.2 were obtained. The properties measurements on the sintered cold pressed pellets showed better power factor and competitive ZT value (0.32 at 575 K for the cold pressed $Pb_{0.9}Bi_{2.1}Te_4$ in comparison with 0.5 at 600 K for the hot pressed $PbBi_2Te_4$). A strong evidence was obtained and indicated that the existence of $PbBi_4Te_7$ and $PbBi_6Te_{10}$. In addition to the two ternary compounds shown in this work, the properties of the $Pb_{1-x}Bi_{2+x}Te_4$ series can be further improved by more doping work with more x values between 0.15 and 0.25. Hot pressing can improving the properties measurements. Both pure phases of the $PbBi_4Te_7$ and $PbBi_6Te_{10}$ type compounds need to be synthesized to explore the ternary system.

The $Tl_{8.67}Pb_xBi_{1.33-x}Te_6$ representatives with x = 0.50 – 1.0 were successfully synthesized and the properties of the series are comparable to the published results of Tl_9BiTe_6 (ZT ≈ 0.57 for $Tl_{8.67}Pb_{0.60}Bi_{0.73}Te_6$ at 575 K). However, hot pressed pellets are needed for the thermal diffusivity measurements. In the future, zone refined technique can be used to enhance the purity of the compounds and therefore better properties.

References

(1) http://unfccc.int/meetings/cop_15/items/5257.php.

(2) Masters, G. M. *Renewable and Efficient Electric Power Systems*; John Wiley & Sons, Inc: Hoboken, NJ., **2004**.

(3) Johansson, T. B. *Renewable Energy: Sources for Fuel and Electricity*; Island Press: Washington, D. C., **1993**.

(4) Winter, M.; Brodd, R. J. *Chem. Rev.* **2004**, *104*, 4245.

(5) Rowe, D. M. In *Thermoelectrics Handbook: Macro to Nano*; Rowe, D. M., Ed.; CRC Press: Boca Raton, FL., **2006**, p 1-2.

(6) Nolas, G. S.; Sharp, J.; Goldsmid, H. J. In *Thermoelectircs, Basic Principles and New Materials Developments*; Springer: Verlag, Berlin, Heidelberg, **2001**, p 5.

(7) Fleurial, J.-P. *Global Innovation: Materials for Energy* **2009**, *61*, 79.

(8) Yang, J.; Caillat, T. *Mater. Res. Bull.* **2006**, *31*, 224.

(9) Snyder, G. J.; Toberer, E. S. *Nature Mater.* **2008**, *7*, 105.

(10) Ghamaty, S.; Bass, J. C.; Elsner, N. B. In *Thermoelectrics Handbook: Macro to Nano*; Rowe, D. M., Ed.; CRC Press: Boca Raton, FL., **2006**, p 57-9-57-11.

(11) Leavitt, F. A.; Elsner, N. B.; Bass, J. C. *Proc. Intern. Conf. Thermoelectr.* **1996** *15*, 378

(12) DiSalvo, F. J. *Science* **1999**, *285*, 703.

(13) Ghamaty, S.; Bass, J. C.; Elsner, N. B. In *Thermoelectrics Handbook: Macro to Nano*; Rowe, D. M., Ed.; CRC Press: Boca Raton, FL., **2006**, p 57-1-57-9.

(14) Thacher, E. F.; Helenbrook, B. T.; Karri, M. A.; Richter, C. J. *Proceedings of the Institution of Mechanical Engineers, Part D: J. Automobile Engineering* **2007**, *211*, 95.

(15) Bass, J. C.; Kushch, A. S.; Elsner, N. B. *Proc. Intern. Conf. Thermoelectr.* **2001**, *20*, 1.

(16) http://www.sunnerelectric.en.alibba.com.

(17) Nolas, G. S.; Sharp, J.; Goldsmid, H. J. In *Thermoelectircs, Basic Principles and New Materials Developments*; Springer: Verlag, Berlin, Heidelberg, **2001**, p 12-13.

(18) Nolas, G. S.; Sharp, J.; Goldsmid, H. J. In *Thermoelectircs, Basic Principles*

and New Materials Developments; Springer: Verlag, Berlin, Heidelberg **2001**, p 74-75.

(19) Mott, N. F.; Jones, H. *The Theory of the Properties of Metals and Alloys*; Dover Publicaitons Inc.: New York, N. Y., **1958**.

(20) Mahan, G. D.; Sofo, J. O. In *Proc. Natl. Acad. Sci.* U.S.A., **1990**; Vol. 93, p 7436.

(21) Yang, J. In *Thermal Conductivity: Theory, Properties, and Applications*; Tritt, T. M., Ed.; Kluwer Academic/Plenum Publishers: New York, N. Y. , **2004**, p 9-10.

(22) Slack, G. A. In *CRC Handbook of Thermoelectrics*; Rowe, D. M., Ed.; CRC Press: Boca Raton, FL., **1995**, p 407-440.

(23) Slack, G. A. *Solid State Physics*; Academic Press: New York, NY., **1979**.

(24) Nolas, G. S.; Poon, J.; Kanatzidis, M. G. *Mat. Res. Bull.* **2006**, *31*, 199.

(25) Nolas, G. S.; Sharp, J.; Goldsmid, H. J. In *Thermoelectrics, Basic Principles and New Materials Developments*; Springer: New York, N. Y., **2001**.

(26) Skrabek, E. A.; Trimmer, D. S. In *CRC Handbook of Thermoeelctrics*; Rowe, D. M., Ed.; CRC Press: Boca Raton, FL., **1995**, p 267.

(27) Chung, D.-Y.; Hogan, T.; Brazis, P.; Rocci-Lane, M.; Kannewurf, C.; Bastea, M.; Uher, C.; Kanatzidis, M. G. *Science* **2000**, *287*, 1024.

(28) Sales, B. C.; Mandrus, D.; Williams, R. K. *Science* **1996**, *272*, 1325.

(29) Nolas, G. S.; Kaeser, M.; Littleton, R. T. I.; Tritt, T. M. *Appl. Phys. Lett.* **2000**, *77*, 1855.

(30) Dyck, J. S.; Chen, W.; Uher, C.; Chen, L.; Tang, X.; Hirai, T. *J. Appl. Phys.* **2002**, *91*, 3698.

(31) Tang, X. F.; Chen, L. D.; Wang, J.; Zhang, Q. J.; Goto, T.; Hirai, T. *J. Alloys Compd.* **2005**, *394*, 259.

(32) Puyet, M.; Dauscher, A.; Lenoir, B.; Dehmas, M.; Stiewe, C.; Müller, E. *J. Appl. Phys.* **2005**, *97*, 083712/1.

(33) Kim, W.; Zide, J.; Gossard, A.; Klenov, D.; Stemmer, S.; Shakouri, A.; Majumdar, A. *Phys. Rev. Lett.* **2006**, *96*, 045901.

(34) Hsu, K. F.; Loo, S.; Guo, F.; Chen, W.; Dyck, J. S.; Uher, C.; Hogan, T.; Polychroniadis, E. K.; Kanatzidis, M. G. *Science* **2004**, *303*, 818.

(35) Poudeu, P. F. P.; D'Angelo, J.; Kong, H.; Downey, A.; Short, J. L.; Pcionek, R.;

Hogan, T. P.; Uher, C.; Kanatzidis, M. G. *J. Am. Chem. Soc.* **2006**, *128*, 14347.

(36) Khitun, A.; Wang, K. L.; Chen, G. *Nanotechnol.* **2000**, *11*, 327.

(37) Yoder, M. N. In *Synthetic Diamond: Emerging CVD Science and Technology*; Spear, H. E., Dismuhes, J. P., Eds.; John Wiley & Sons, Inc.: New York, NY., **1994**, p 3-13.

(38) West, A. R. In *Solid State Chemistry and Its Application*; 4th ed.; John Wiley and Sons, Inc.: New York, NY., **1990**, p 5-16.

(39) Smart, L. E.; Moore, E. A. In *Solid State Chemistry: an Introduction*; 3rd ed.; CRC press: Boca Raton, FL., **2005**, p 142-149.

(40) Schubert, U.; Hüsing, N. *Synthesis of Inorganic Materials*; 2nd ed.; Wiley-VCH: Weinheim, Germany, **2005**.

(41) Sun, D. C.; Senz, S.; Hesse, D. *J. Eur. Ceram. Soc.* **2006**, *26*, *3181*.

(42) West, A. R. In *Solid State Chemistry and Its Application*; 4th ed.; John Wiley and Sons, Inc.: New York, NY., **1990**, p 115-123.

(43) Suryanarayana, C.; Norton, M. G. In *X-Ray Diffraction: a Practical Approach*; Plenum Press: New York, NY., **1998**, p 5-6.

(44) He, B. B. In *Two-Dimensional X-Ray Diffraction*; John Wiley and Sons Inc.: Hoboken, NJ., **2009**, p 66-67.

(45) Bonnelle, C.; Jonnard, P.; André, J.-M.; Avila, A.; Laporte, D.; Ringuenet, H.; Lépy, M. C.; Plagnard, J.; Ferreux, L.; Protas, J. C. *Nucl. Instrum. Methods Phys. Res., Sect. A: Accelerators, Spectrometers, Detectors and Associated Equipment* **2004**, *516*, 594.

(46) Smart, L. E.; Moore, E. A. In *Solid State Chemistry: an Introduction*; 3rd ed.; CRC press: Boca Raton, FL., **2005**, p 77-82.

(47) He, B. B. In *Two-Dimensional X-Ray Diffraction*; John Wiley and Sons Inc.: Hoboken, NJ., **2009**, p 18-21.

(48) Massa, W. *Crystal Structure Determination*; 2nd ed.; Springer: Heidelberg, **2004**.

(49) West, A. R. In *Solid State Chemistry and Its Application*; 4th ed.; John Wiley and Sons, Inc.: New York, NY., **1990**, p 144-169.

(50) He, B. B. In *Two-Dimensional X-Ray Diffraction*; John Wiley and Sons Inc.:

Hoboken, NJ., **2009**, p 85-90.

(51) Peterson, V. K. *Powder Diffr.* **2005**, *20*, 14.

(52) Larson, A. C.; Dreele, R. B. v.; Los Alamos National Laboratory: Los Alamos, NM, **2000**.

(53) Xu, J.; Sonne, M.; Yanangiya, S.-i.; Nong, N. V.; Pryds, N.; Nygren, M.; Kleinke, H. *J. Alloys Compd.* **2010**, *210*, 183.

(54) http://www.ulvac.com/thermal/zem%203.asp.

(55) Schroder, D. K. In *Semiconductor Material and Device Characterization*; 3rd ed.; John Wiley & Sons, Inc.: Hoboken, NJ., **2006**, p 2-8.

(56) Murti, P. S. In *Laser Applications in Material Science and Industry*; kesavamoorthy, R., Arora, A. K., Rao, C. B., Kalyanasundaram, P., Eds.; Allied Publishers: New Delhi, **1997**, p 77-80.

(57) http://anter.com/TN68.htm.

(58) Parker, W. J.; Jenkins, W. J.; Butler, C. P.; Abbott, G. L. *J. Appl. Phys.* **1961**, *32*, 1679.

(59) Laing, M. *J. Appl. Phys.* **2006**, *83*, 1499.

(60) Kanatzidis, M. G. *Semicond. Semimet.* **2001**, *69*, 51.

(61) Shelimova, L. E.; Konstantinov, P. P.; Karpinskii, O. G.; Avilov, E. S.; Kretova, M. A.; Zenskov, V. S. *J. Alloys Compd.* **2001**, *329*, 50.

(62) Caillat, T.; Huang, C. K.; Fleurial, J.-P.; Snyder, G. J.; Borshchevsky, A. *Proc. Intern. Conf. Thermoelectr.* **2000**, *19*, 151.

(63) Kuznetsov, V. L.; Kuznetsova, L. A.; Rowe, D. M. *J. Appl. Phys.* **1999**, *85*, 3207.

(64) Kuznetsov, V. L.; Kuznetsova, L. A.; Rowe, D. M. *J. Phys. D: Appl. Phys.* **2001**, *34*, 700.

(65) Oosawa, Y.; Tateno, Y.; Mukaida, M.; Tsunoda, T.; Imai, Y.; Isoda, Y.; Nishida, I. A. *Proc. Intern. Conf. Thermoelectr.* **1999**, *18*, 550.

(66) Golovanova, N. S.; Zlomanov, V. P.; Tananaeva, O. I. *Izv. Akad. Nauk SSSR, Neorg. Mater.* **1983**, *10*, 740.

(67) Hirai, T.; Takeda, Y.; Kurata, K. *J. Less Common Met.* **1967**, *13*, 352.

(68) Chami, R.; Brun, G.; Tedenac, J.-C.; Maurin, M. *Rev. Chim. Miner.* **1983**, *20*,

305.

(69) Skoropanov, A. S.; Valevsky, B. L.; Skums, V. F.; Samal, G. I.; A., V. A. *Thermochim. Acta* **1985**, *90*, 331.

(70) Karpinskii, O. G.; Shelimova, L. E.; Avilov, E. S.; Kretova, M. A.; Zemskov, V. S. *Inorg. Mater.* **2002**, *38*, 17.

(71) Shelimova, L. E.; Karpinskii, O. G.; Konstantinov, P. P.; Avilov, E. S.; Kretova, M. A.; Zemskov, V. S. *Inorg. Mater.* **2004**, *40*, 451.

(72) Zhukova, T. B.; Zaslavskii, A. I. *Sov. Phys. Cryst.* **1972**, *16*, 792.

(73) McGuire, M. A.; Reynolds, T. K.; DiSalvo, F. J. *Chem. Mater.* **2005**, *17*, 2875.

(74) Kurosaki, K.; Kosuga, A.; Muta, H.; Uno, M.; Yamanaka, S. *Appl. Phys. Lett.* **2005**, *87*, 061919.

(75) Kurosaki, K.; Kosuga, A.; Goto, K.; Muta, H.; Yamanaka, S. *Proc. Intern. Conf. Thermoelectr.* **2005**, *24*, 311.

(76) Yamanaka, S.; Kosuga, A.; Kurosaki, K. *J. Alloys Compd.* **2003**, *352*, 275.

(77) Pradel, A.; Tedenac, J.-C.; Coquillat, D.; Brun, G. *Rev. Chim. Miner.* **1982**, *19*, 3.

(78) Pradel, A.; Tedenac, J. C.; Brun, G.; Maurin, M. *Journal of Solid State Chemistry* **1982**, *45*, 99.

(79) Wölfing, B.; Kloc, C.; Teubner, J.; Bucher, E. *Phys. Rev. Lett.* **2001**, *86*, 4350.

(80) Böettcher, P.; Doert, T.; Druska, C.; Bradtmöeller, S. *J. Alloys Compd.* **1997**, *246*, 209.

(81) Doert, T.; Böttcher, P. *Neorg. Mater.* **1988**, *24*, 1479.

(82) Caillat, T.; Kulleck, J.; Borshchevsky, A.; Fleurial, J.-P. *J. Appl. Phys.* **1996**, *79*, 8419

(83) Slack, G. A. *Phys. Rev. Lett.* **1962**, *126*, 427

(84) Nolas, G. S.; Harris, V. G.; Tritt, T. M.; Slack, G. A. *J. Appl. Phys.* **1996**, *80*, 6304.

(85) Cordero, B.; Gomez, V.; Platero-Prats, A. E.; Reves, M.; Echeverria, J.; Cremades, E.; Barragan, F.; Alvarez, S. *Dalton Trans.* **2008**, *21*, 2832.

(86) Marsh, R. E. *J. Solid State Chem.* **1991**, *92*, 594.

(87) Böttcher, P.; Doert, T.; Druska, C.; Bradtmöller, S. *J. Alloys Compd.* **1997**, *246*,

209.

(88) Fleurial, J. P.; Gailliard, L.; Triboulet, R.; Scherrer, H.; Scheerer, S. *J. Phys. Chem. Solids* **1988**, *59*, 1237.